

Chapter 7: Couplings Between Changes in the Climate System and Biogeochemistry Figures

Coordinating Lead Authors: Kenneth L. Denman (Canada), Guy Brasseur (USA, Germany)

Lead Authors: Amnat Chidthaisong (Thailand), Philippe Ciais (France), Peter Cox (UK), Robert E. Dickinson (USA), Didier Hauglustaine (France), Christoph Heinze (Norway, Germany), Elisabeth Holland (USA), Daniel Jacob (USA, France), Ulrike Lohmann (Switzerland), Srikanthan Ramachandran (India), Pedro Leite da Silva Dias (Brasil), Steven C. Wofsy (USA), Xiaoye Zhang (China)

Contributing Authors: David Archer (USA), Vivek Arora (Canada), John Austin (USA), David Baker (USA), Joe Berry (USA), Richard A. Betts (UK), Gordon Bonan (USA), Philippe Bousquet (France), Josep Canadell (Australia), James Christian, Deborah A. Clark (USA), Martin Dameris (Germany), Franck Dentener (EU), David Easterling (USA), Veronika Eyring (Germany), Johann Feichter (Germany), Pierre Friedlingstein (France, Belgium), Inez Fung (USA), Sandro Fuzzi (Italy), Sunling Gong (Canada), Nicolas Gruber (USA, Switzerland), Alex Guenther (USA), Kevin Gurney (USA), Ann Henderson-Sellers (Australia), Joanna House (UK), Andy Jones (UK), Christopher Jones (UK), Bernd Kärcher (Germany), Michio Kawamiya (Japan), Keith Lassey (New Zealand), Caroline Leck (Sweden), Julia Lee-Taylor (USA, UK), Corinne Le Quéré (Germany, France, Canada), Gordon McFiggans (UK), Yadvinder Malhi (UK), Kenneth Masarie (USA), Surabi Menon (USA), John B. Miller (USA), Philippe Peylin (France), Andrew Pitman (Australia), Johannes Quaas (Germany), Michael Raupach (Australia), Peter Rayner (Australia), Gregor Rehder (Germany), Ulf Riebesell (Germany), Christian Rödenbeck (Germany), Leon Rotstayn (Australia), Nigel Roulet (Canada), Christopher Sabine (USA), Martin G. Schultz (Germany), Michael Schulz (France, Germany), Stephen E. Schwartz (USA), Will Steffen (Australia), David Stevenson (UK), Yuhong Tian (USA, China), Kevin E. Trenberth (USA), Twan Van Noije, Oliver Wild (Japan, UK), Tingjun Zhang (USA, China), Liming Zhou (USA, China)

Review Editors: Kansri Boonpragob (Thailand), Martin Heimann (Germany, Switzerland), Mario Molina (USA, Mexico)

Date of Draft: 27 October 2006

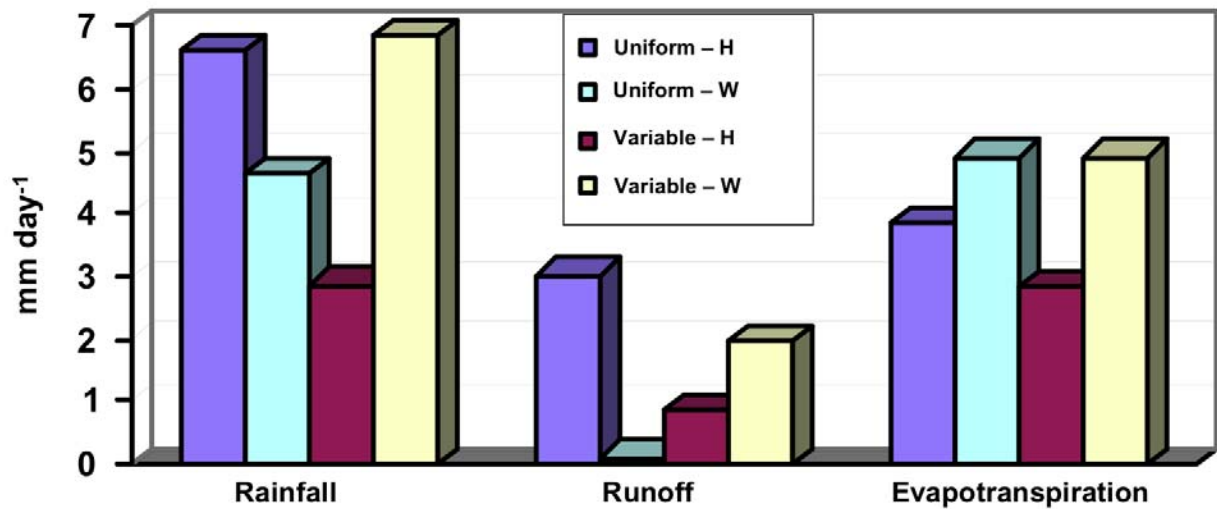
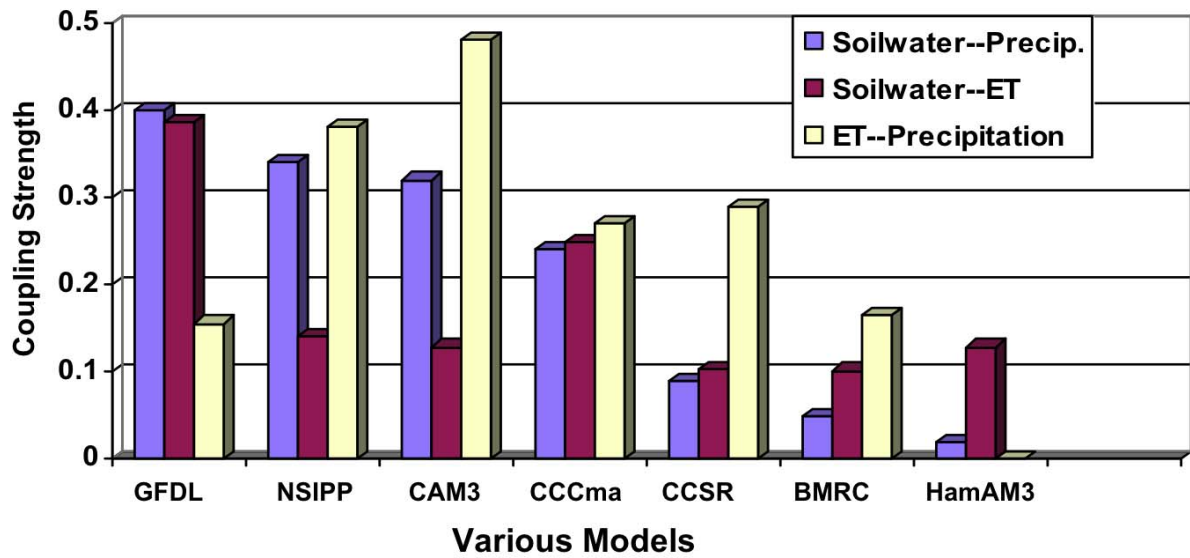
1
23
4
5
6
7
8
9
10
11
12
13
14

Figure 7.1. Derived from climate simulation results given in Table 3 of Hahmann (2004) denoted H and Figure 1 of Wang and Eltahir (2000) denoted W. Hahmann's results are for the Amazon centered on the equator and Wang and Eltahir's for Africa at the equator. Both studies have examined the differences for precipitation 'uniform' over a model grid-square versus added to about 10% of the grid-square (denoted 'variable'). Large differences are seen between the two cases of the opposite sense for the two studies: precipitation shows a large reduction for the Hahmann variable case relative to uniform whereas an increase is seen for the Wang and Eltahir variable case; the differences are even greater for runoff where Hahmann's uniform case runoff is 3 times as large as the variable case, whereas Wang and Eltahir have almost no runoff for their uniform case.

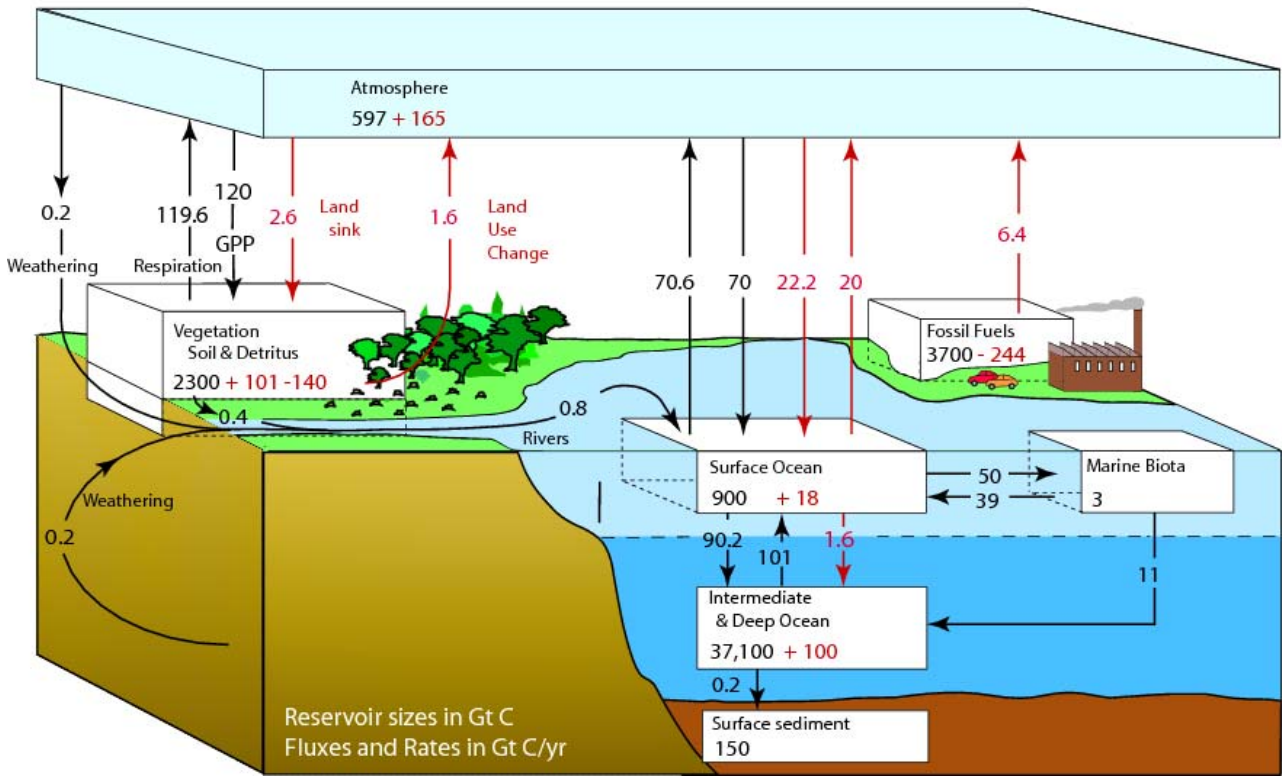
1
2



3
4
5
6
7
8
9
10

Figure 7.2. Drawn from the GLACE study (Table 1 in Guo et al., 2006). The paper compares different climate models as to how strongly their soil water causes summer rainfall. This coupling is divided into how strongly soil water causes evaporation (including from plants) and how strongly this evaporation causes rainfall. The soil water-precipitation coupling is scaled by a factor of 10, and their two indices for evaporation to precipitation coupling are averaged.

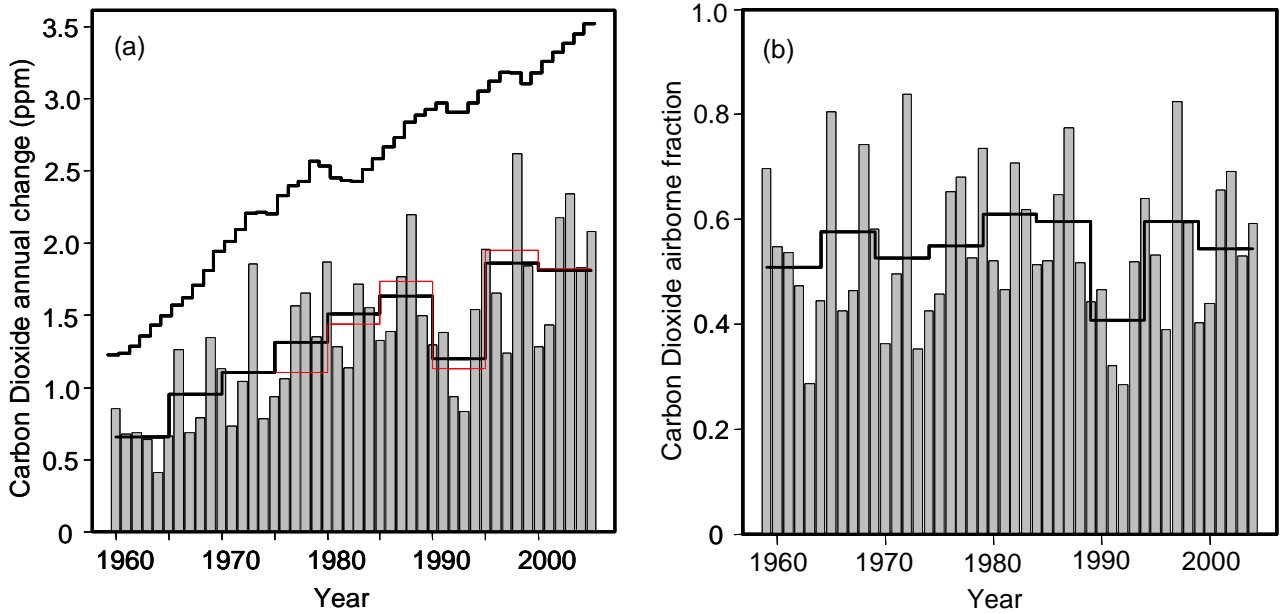
1
2



3
4
5
6
7
8
9
10
11
12
13
14
15
16

Figure 7.3. The global carbon (dioxide) cycle for the 1990s, showing main annual fluxes in GtC yr⁻¹: preindustrial 'natural' fluxes in black and 'anthropogenic' fluxes in red. Modified from Sarmiento and Gruber (2006), with changes in poolsizes from Sabine et al. (2004a). The net terrestrial loss of -39 GtC is inferred from cumulative (fossil fuel emissions - atmospheric increase - ocean storage). The loss of -140 GtC from the 'Vegetation, Soil & detritus' compartment represents the cumulative emissions from land use change (Houghton, 2003), and requires a terrestrial biosphere sink of 101 GtC (in Sabine et al., given only as ranges of -140 to -80 GtC and 61 to 141 GtC respectively; other uncertainties given in their Table 1). Net anthropogenic exchanges with the atmosphere are taken from Column 5 'AR4' in Table 7.1. Gross fluxes generally have uncertainties of more than ±20% but fractional amounts have been retained to achieve overall balance when including estimates in fractions of GtC yr⁻¹ for riverine transport, weathering, deep ocean burial, etc. 'GPP' is annual gross (terrestrial) primary production.

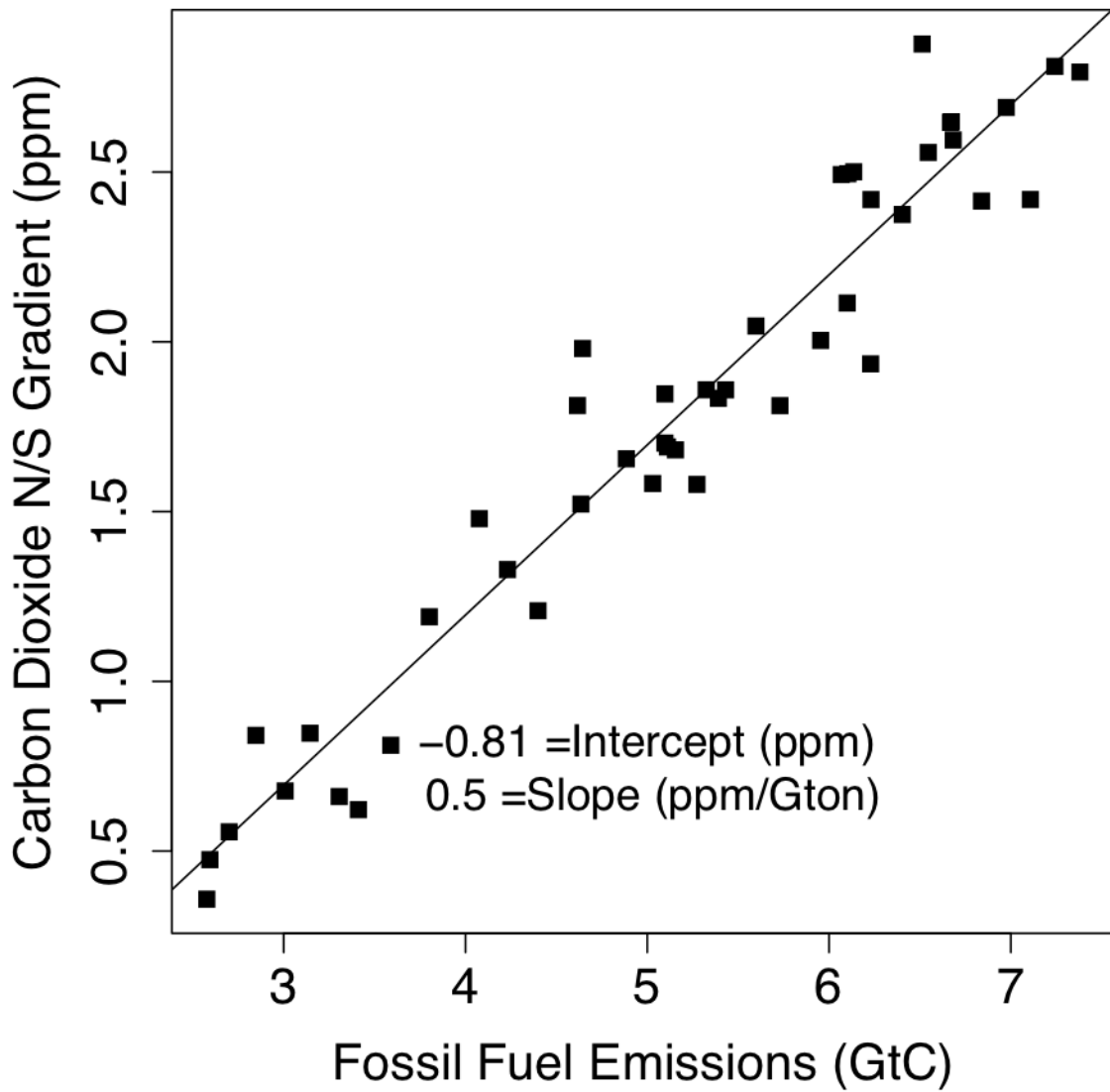
1
2



3
4
5
6
7
8
9
10
11
12
13
14

Figure 7.4. Changes in global atmospheric CO₂ concentrations: (a) annual changes (*bars*) and 5-yr means (*black lines*), of global CO₂ concentrations, from Scripps Institution of Oceanography observations (mean of South Pole and Mauna Loa; Keeling and Whorf, 2005, updated); (*upper -*): annual increases that would occur if 100% of fossil fuel emissions (Marland et al, 2006, updated as described in Ch. 2) stayed in the atmosphere; and (*red line*) 5-yr mean annual increases from NOAA data (mean of Samoa and Mauna Loa, Tans and Conway, 2005, updated); (b) Fraction of fossil fuel emissions remaining in the atmosphere each year ('Airborne fraction', **I**), 5-yr mean (*line -*) (Scripps data), and mean since 1958 (*---*). Note (↓) the anomalously low airborne fraction in the early 1990s.

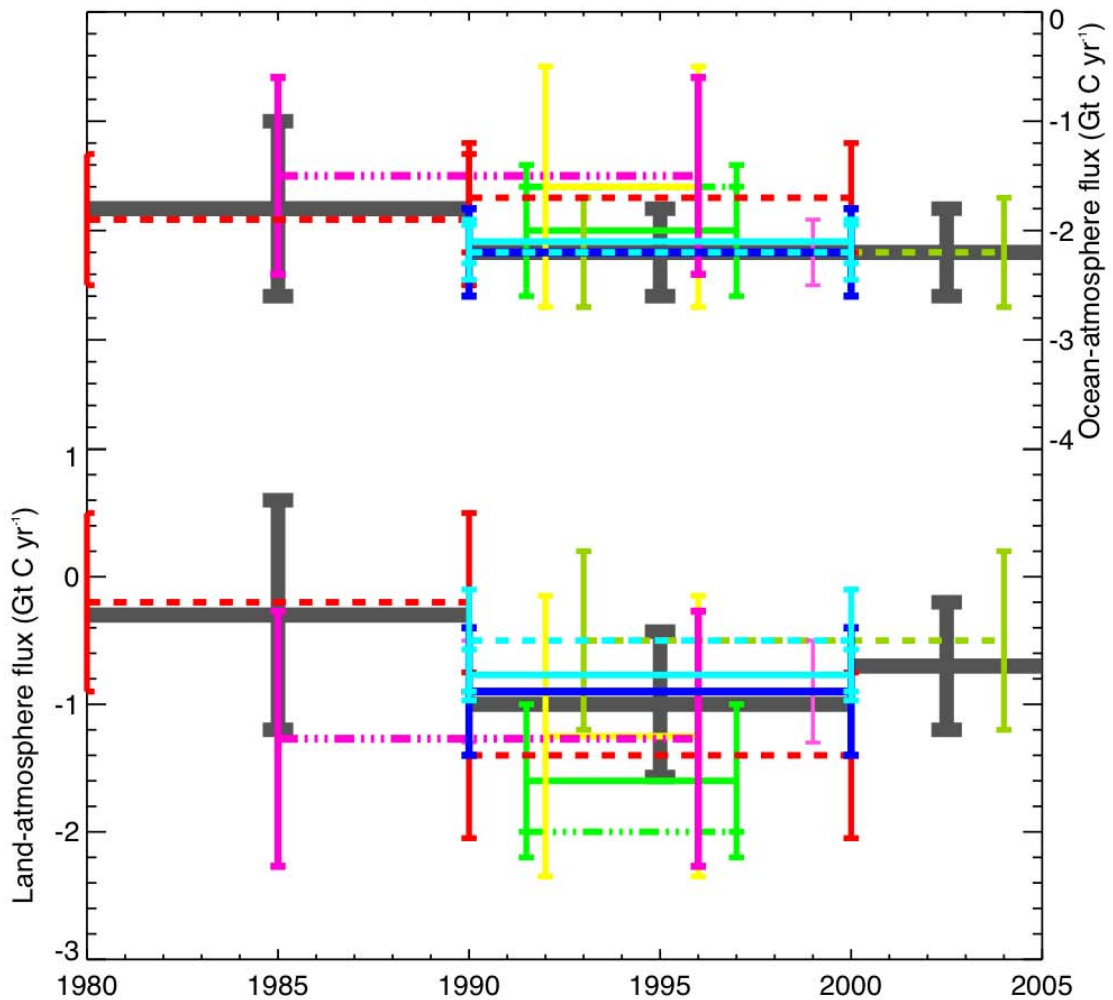
1
2



3
4
5 **Figure 7.5.** North-south CO₂ concentration difference is shown on the Y-axis, computed as the difference of
6 annual mean concentrations (ppm) at Mauna Loa and South Pole (Keeling and Whorf, 2005, updated), and is
7 plotted against annual fossil fuel emission flux (GtC) (Marland, et al., 2006) on the X-axis, with a line showing
8 the best fit. The observations show that the North-South difference in CO₂ increase proportionally with fossil
9 fuel use, verifying the global impact of human-caused emissions.
10

1
2

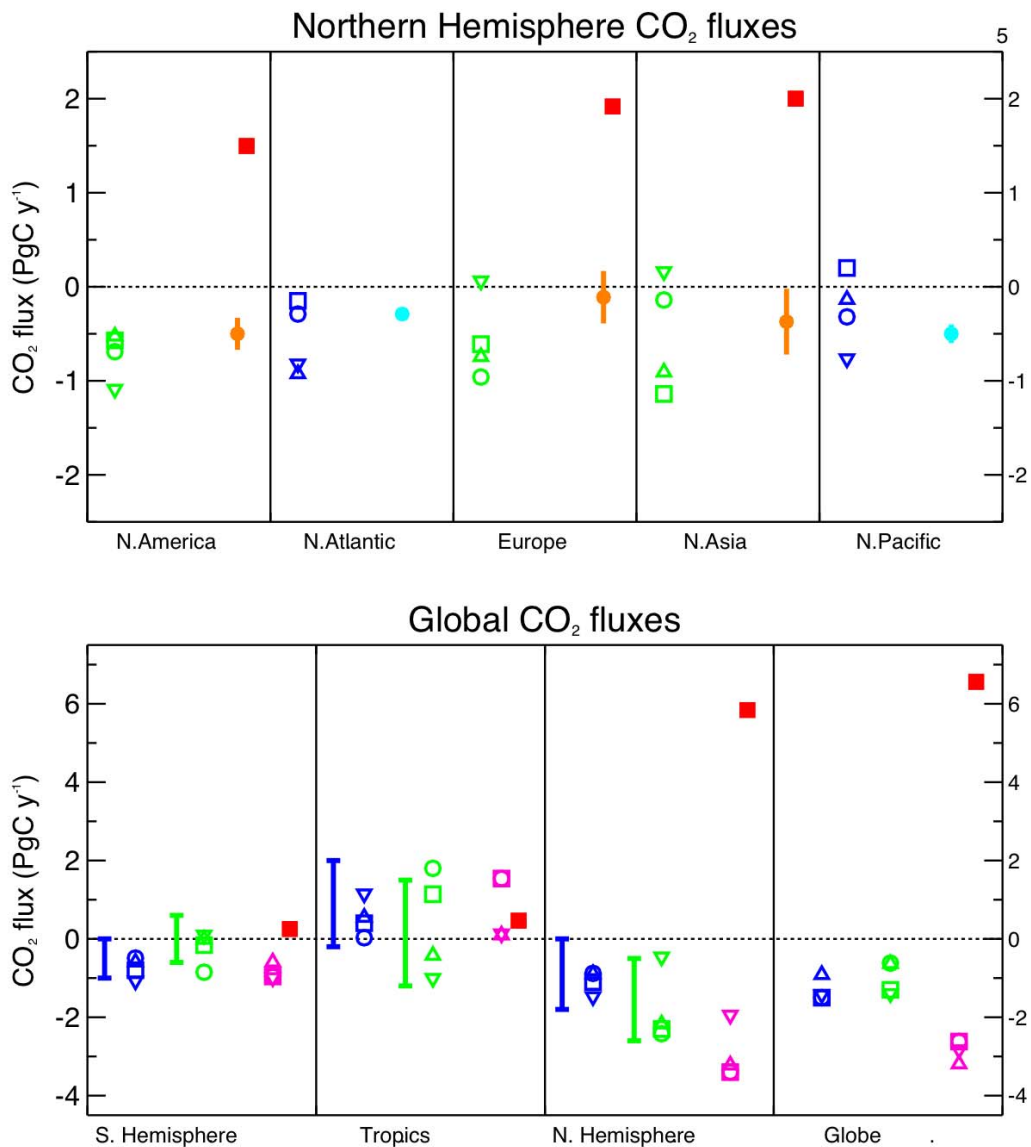
- AR4 1980s updated from TAR
- AR4 1990s
- AR4 early 2000s
- Atmospheric CO₂ and ¹³C [Battle et al. 2000]
- Atmospheric CO₂ and O₂/N₂ [Battle et al. 2000]
- - Atmospheric CO₂ and O₂/N₂ [Manning and Keeling, 2005]
- Atmospheric inversions Transcom [Gurney et al. 2002]
- Ocean change in CFC inventory [McNeil et al. 2002]
- Ocean ¹³C disequilibrium [Gruber and Keeling 2001]
- - TAR 1980s atmospheric O₂/N₂ trends [Prentice et al. 2001]
- - TAR 1990s atmospheric O₂/N₂ trends [Prentice et al. 2001]
- Ocean pCO₂ surveys, [Takahashi et al. 2002]
- Joint ocean-atmosphere inversion [Jacobson et al. 2006]
- - Ocean inversion anthropogenic carbon [Mikaloff-Fletcher, 2006]



3
4
5
6
7
8

Figure 7.6. Individual estimates of the ocean-atmosphere flux reported in Chapter 5 and of the pertaining land-atmosphere required to close the global carbon budget. The dark thick lines are the revised budget estimates in the AR4 for the 1980's, the 1990's and the early 2000's respectively.

1
2



3
4
5
6
7
8
9
10
11
12
13
14
15
16
17
18
19
20

Figure 7.7. Regional ocean-atmosphere and land-atmosphere CO₂ fluxes from inversion ensembles and bottom-up studies. Fluxes to the atmosphere are positive and uptake has negative sign. Inversion results all correspond to the post-Pinatubo period 1992–1996. Top Panel: Regional Northern Hemispheric carbon fluxes. Bottom Panel: Regional fluxes over latitude bands and the globe. *Orange*: Bottom-up terrestrial fluxes from Pacala et al. (2001) and Kurz and Apps (1999) for North America, from Janssens et al. (2003) for Europe, and Shvidenko and Nilsson (2003) plus Fang et al. (2001) for North Asia (Asian Russia and China). *Cyan*: Bottom-up ocean flux estimates from Takahashi, et al., (2002). *Blue*: ocean fluxes from atmospheric inversions, *Green*: terrestrial fluxes from inversion models. *Magenta*: total inversion fluxes, *Red*: fossil fuel emissions. The mean flux of different inversion ensembles is reported. Inversion errors on regional fluxes are not reported here; Their values are usually comprised between 0.5 and 1 GtC yr⁻¹. *Error bar*: range of atmospheric inversion fluxes from the TAR. *Squares*: Gurney et al. (2002) inversions using annual mean CO₂ observations and 16 transport models. *Circles*: Gurney et al. (2003) inversions using monthly CO₂ observations and 13 transport models. *Triangles*: Peylin et al. (2005) inversions with grey 3 transport models, 3 regional breakdowns and 3 inversion settings. *Inverted triangles*: Rödenbeck et al. (2003a) inversions where the fluxes are solved on the model grid using monthly flask data.

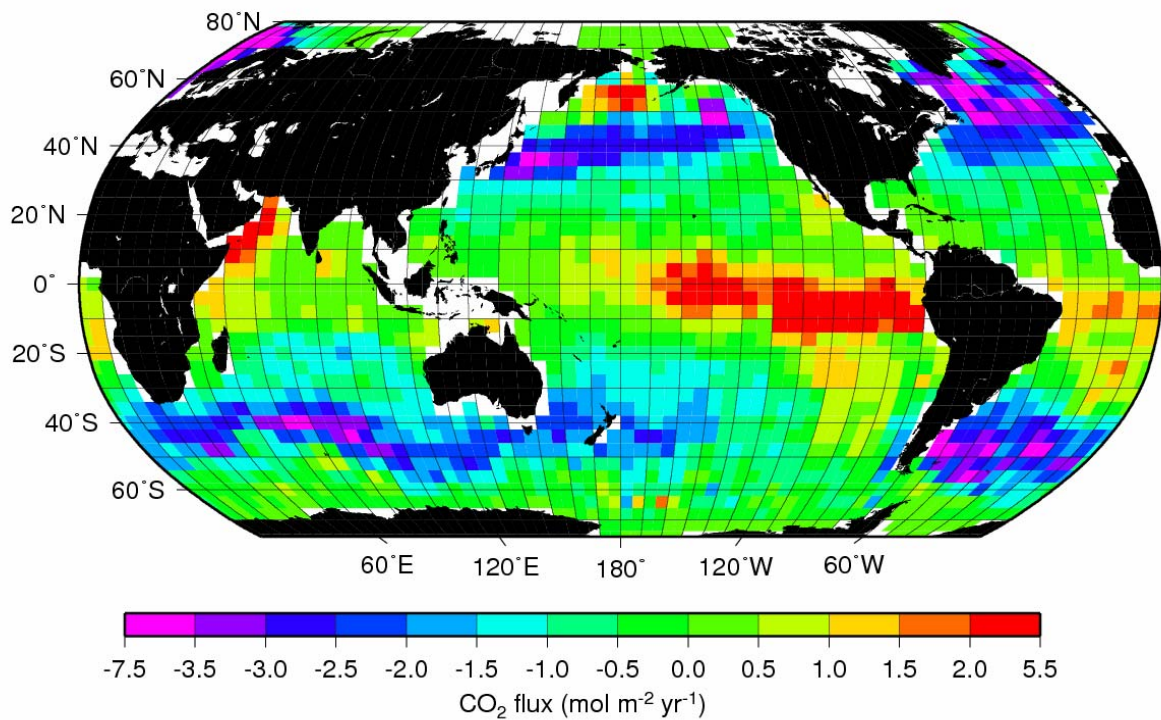
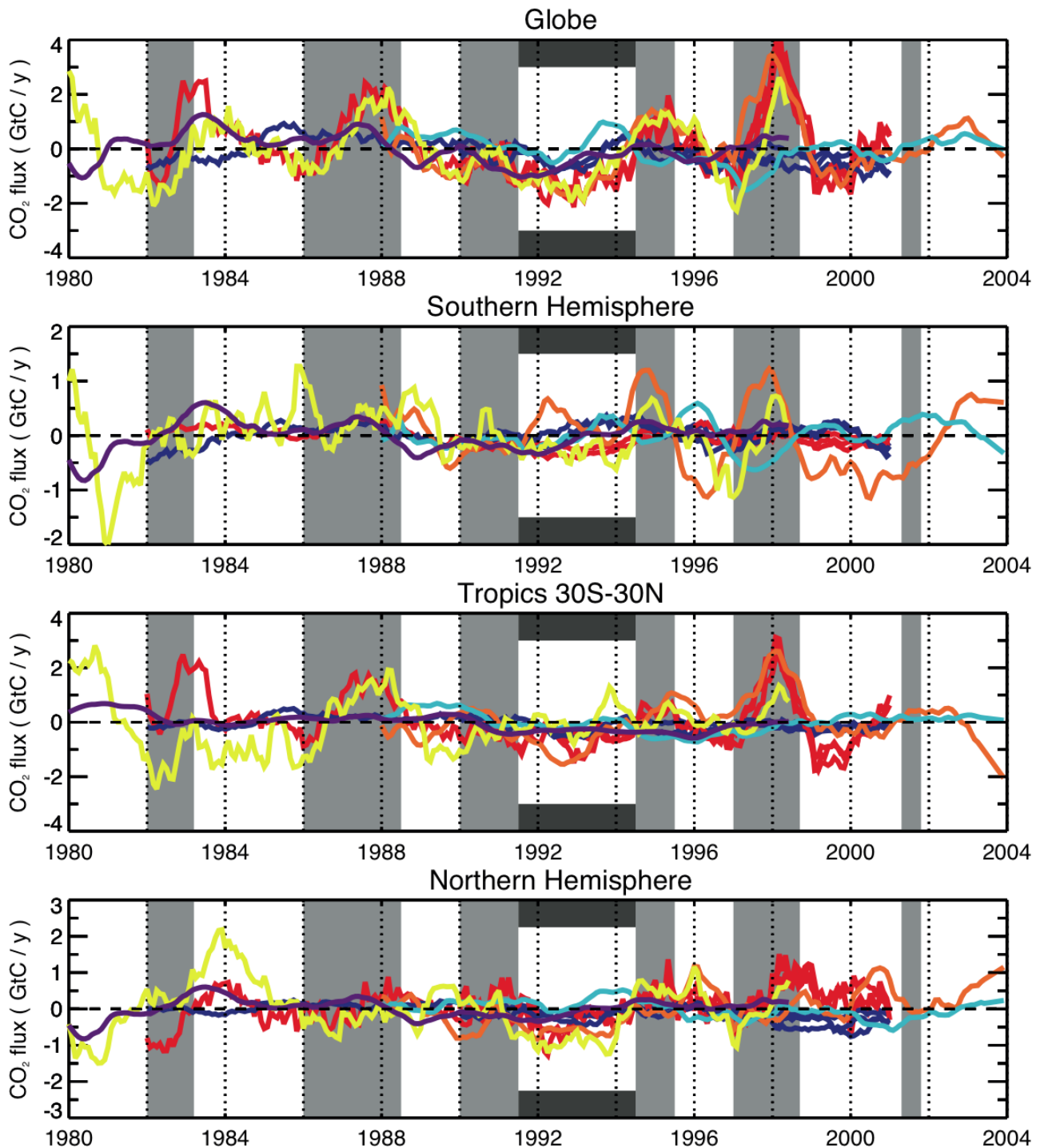
1
23
4
5
6
7
8
9
10
11
12
13
14
15
16

Figure 7.8. The $4^\circ \times 5^\circ$ estimates of sea-to-air flux of CO₂ shown here have been computed using 940,000 measurements of surface water pCO₂ collected since 1956 and averaged monthly, together with NCEP/NCAR 41-year mean monthly wind speeds and a (10-m wind speed)² dependence on the gas transfer rate (Wanninkhof, 1992). The fluxes have been normalized to the year 1995, using techniques described in Takahashi et al. (2002), who had used wind speeds taken at the 0.995 sigma level (about 40 m above the sea surface). The annual flux of CO₂ for 1995 with 10-m winds is -1.6 GtC yr^{-1} , with an approximate uncertainty (see Footnote 1) of $\pm 1 \text{ GtC yr}^{-1}$ mainly due to uncertainty in the gas exchange velocity and limited data coverage. This estimated global flux consists of an uptake of anthropogenic CO₂ of -2.2 GtC yr^{-1} (see text) plus an outgassing of 0.6 GtC yr^{-1} , corresponding primarily to oxidation of organic carbon borne by rivers (Figure 7.3). The monthly flux values with 10-m winds used here are available from T. Takahashi at [http://www.ldeo.columbia.edu/res/pi/CO2/carbondioxide/pages/air_sea_flux_rev1.html].

1
2

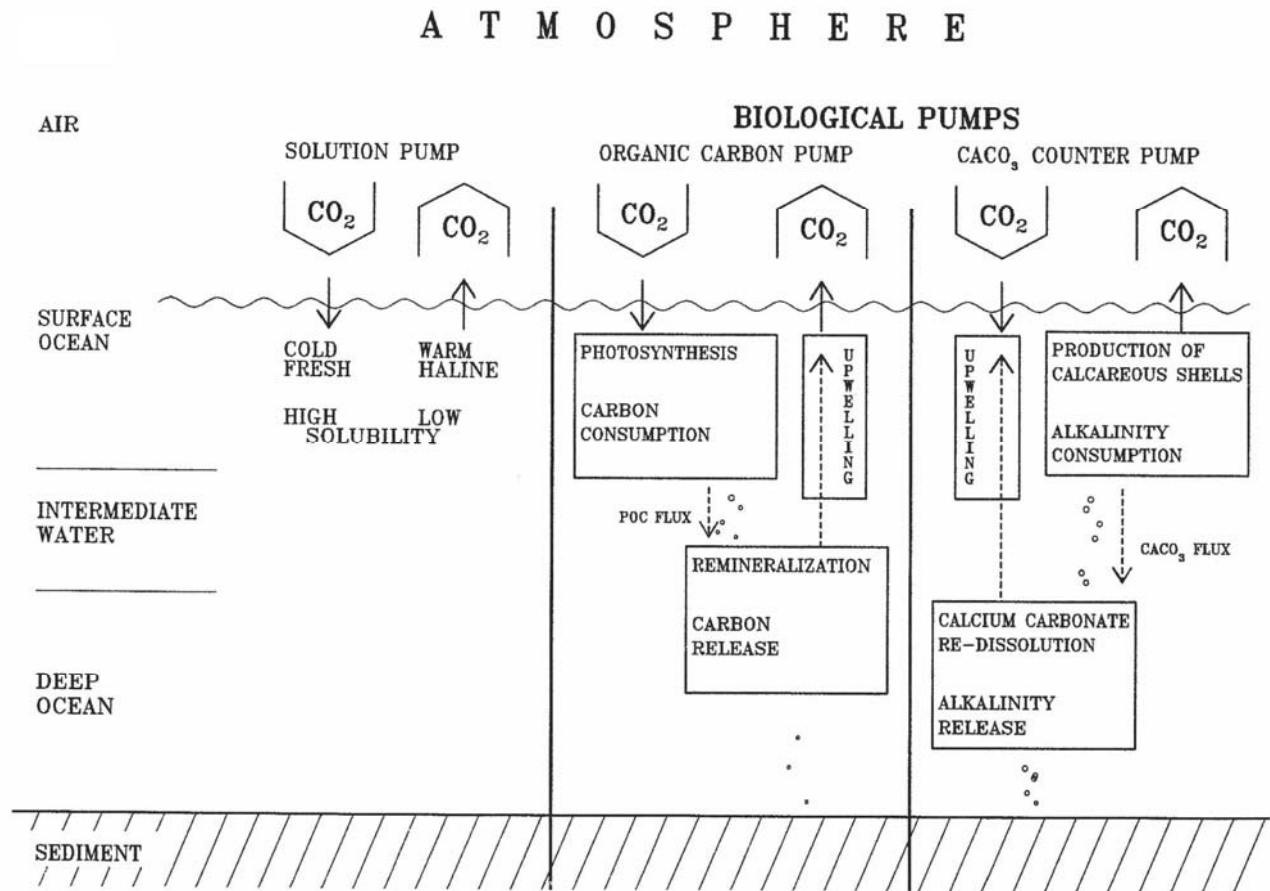
Baker et al. 2005 (orange = land ; cyan = ocean)
 Rodenbeck et al. 2003 (red = land ; blue = ocean)
 Bousquet et al. 2000 + (yellow = land ; purple = ocean)



3
4
5
6
7
8
9
10
11

Figure 7.9. Ocean-atmosphere and land-atmosphere CO₂ fluxes year-to-year anomalies in GtC yr⁻¹, from interannual inversions ensembles covering the past 20 years or so, grouped into large latitude bands, and over the globe. Three different inversion ensembles from Bousquet et al. (2000), Rödenbeck et al. (2003a), and Baker et al. (2006) are shown. For each flux and each region, the anomalies were obtained by subtracting the long-term mean flux and removing the seasonal signal. Gray shaded regions indicate El Niño episodes, and the black bars indicates the cooling period following the Mt. Pinatubo eruption.

1
2



3
4
5
6
7
8
9
10
11
12
13
14
15
16

Figure 7.10. Three main ocean carbon pumps govern the regulation of natural atmospheric CO₂ changes by the ocean (Heinze et al., 1991¹): the solubility pump, the organic carbon pump, and the CaCO₃ 'counter pump'. The oceanic uptake of anthropogenic CO₂ is dominated by inorganic carbon uptake at the ocean surface and physical transport of anthropogenic carbon from the surface to deeper layers. For a constant ocean circulation, to first order, the biological carbon pumps remain unaffected because nutrient cycling does not change. If the ocean circulation slows down, anthropogenic carbon uptake is dominated by inorganic buffering and physical transport as before, but the marine particle flux can reach greater depths if its sinking speed does not change, leading to a biologically-induced negative feedback that is expected to be smaller than the positive feedback associated with a slower physical downward mixing of anthropogenic carbon.

¹ Reprinted with permission, copyright 1991 American Geophysical Union.

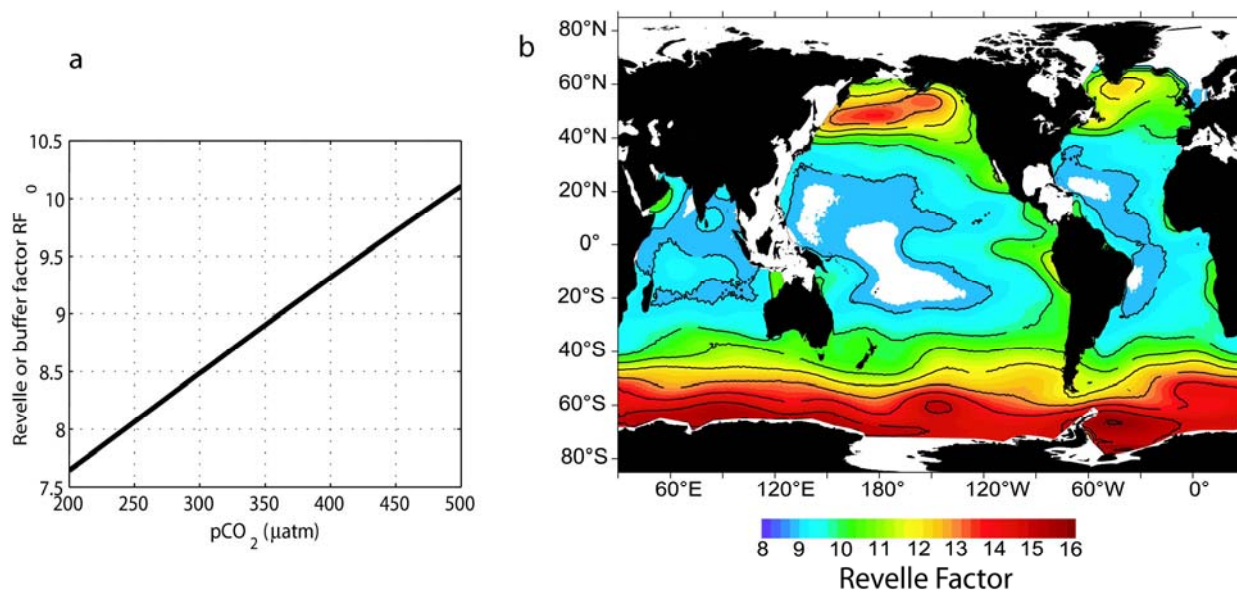
1
23
4
5
6
7
8
9
10
11

Figure 7.11. (a) The Revelle factor (or buffer factor) as a function of CO_2 partial pressure ($T_C = 25^\circ$, $S = 35$, $\text{TA}_{\text{alk}} = 2300 \mu\text{mol kg}^{-1}$) (Zeebe and Wolf-Gladrow, 2001, page 73)¹. (b) The geographical distribution of the buffer factor in ocean surface waters for year 1994 (Sabine et al., 2004a)². High values indicate a low buffer capacity of the surface waters.

¹ Reprinted with permission, copyright 2001 Elsevier.

² Reprinted with permission, copyright 2004 AAAS.

1

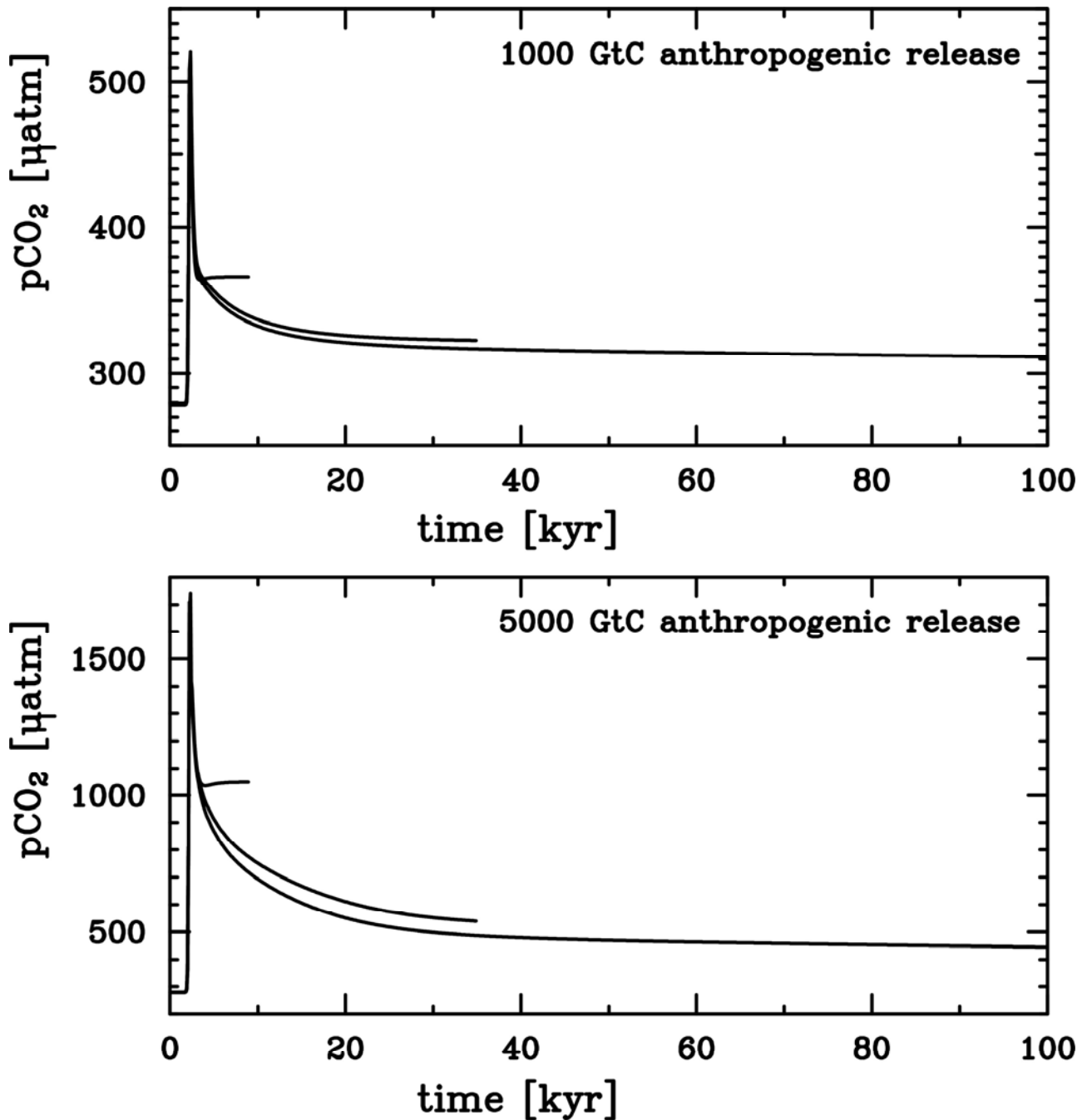
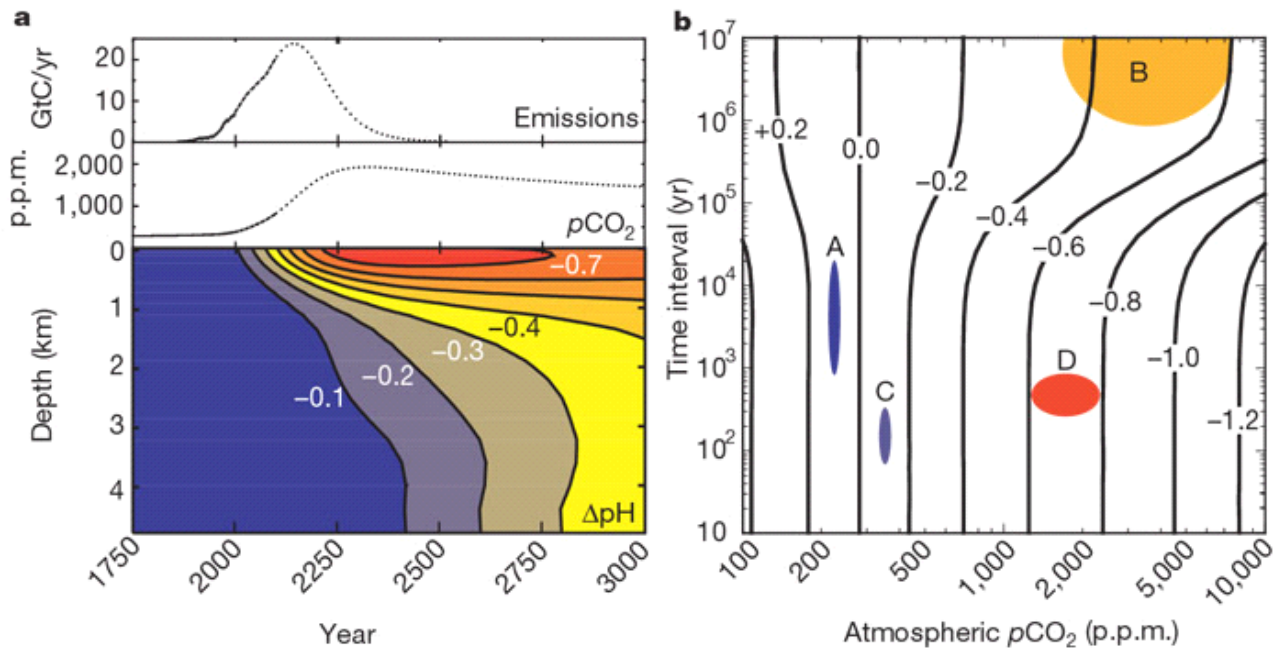
2
3
4
5
6
7
8
9
10

Figure 7.12. Model projections for the neutralization of anthropogenic CO₂ for an ocean-only model, a model including dissolution of CaCO₃ sediment, and a model including in addition weathering of silicate rocks. Top panel: for a total of 1000 GtC of anthropogenic CO₂ emissions. Bottom panel: for a total of 5000 GtC of anthropogenic CO₂. Note that the y-axis is different for the two diagrams! Without CaCO₃ dissolution from the seafloor the buffering of anthropogenic CO₂ is limited. Even after 100,000 years (100 kyr), the remaining CO₂ partial pressure is substantially higher than the preindustrial value. Source: Archer (2005).

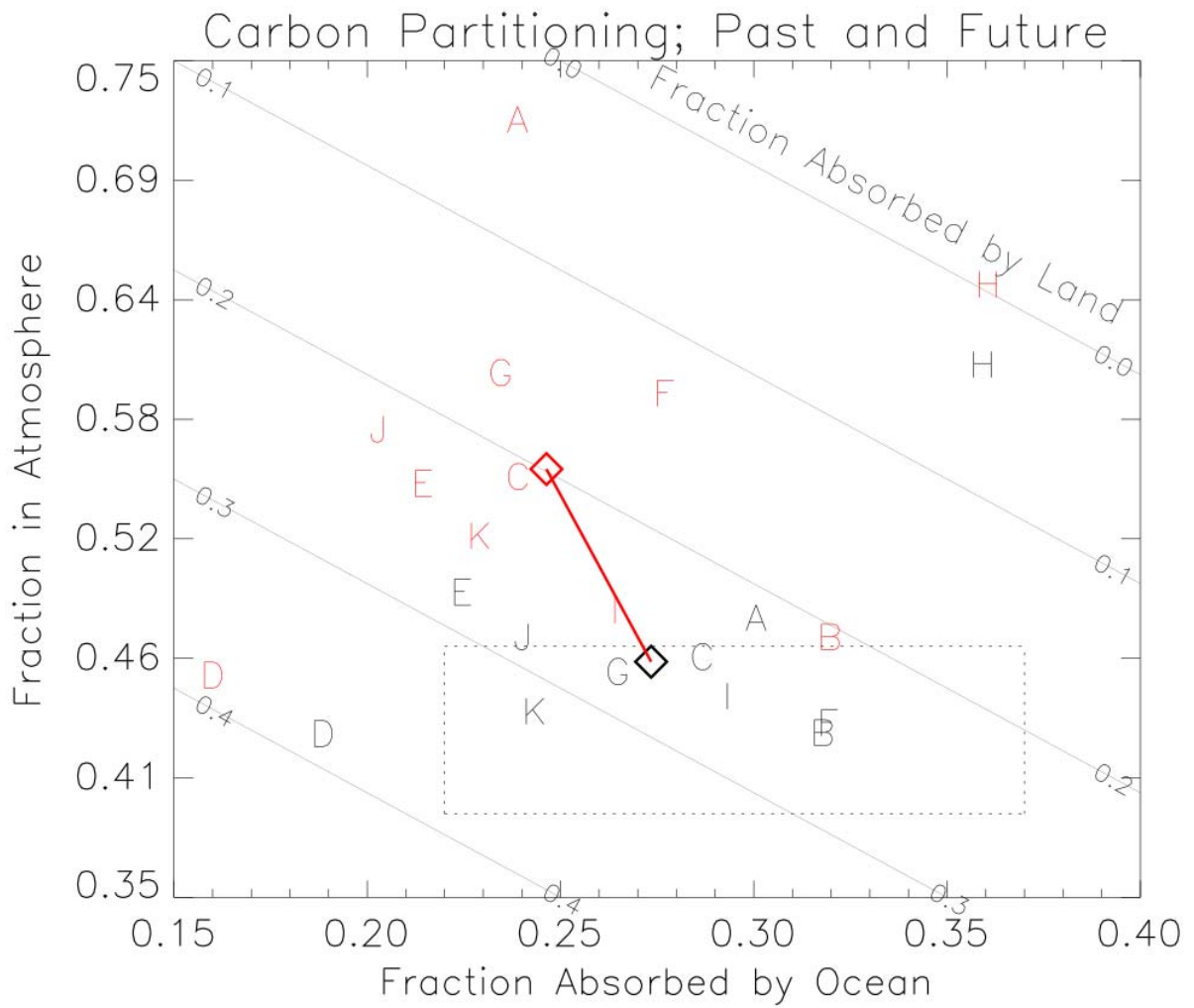
1
2



3
4
5
6
7
8
9
10
11
12
13

Box 7.3, Figure 1. (a) Atmospheric CO₂ emissions, historical atmospheric CO₂ levels and predicted CO₂ concentrations from the given emission time series, together with changes in ocean pH based on horizontally averaged chemistry. The emission time series is based on the mid-range IS92a emission scenario (solid line) prior to 2100 and then assumes that emissions continue until fossil fuel reserves decline. (b) Estimated maximum change in surface ocean pH as a function of final atmospheric CO₂ pressure, and the transition time over which this CO₂ pressure is linearly approached from 280 p.p.m. A: glacial–interglacial CO₂ changes. B: slow changes over the past 300 Myr. C: historical changes in ocean surface waters. D: unabated fossil-fuel burning over the next few centuries. Source: Caldeira and Wickett (2003).

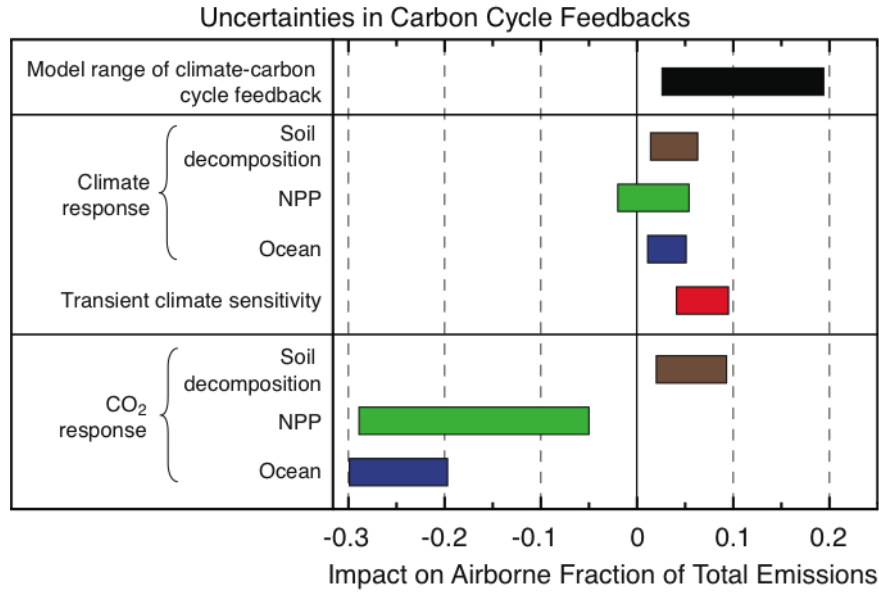
1
2



3
4
5
6
7
8
9
10
11
12
13

Figure 7.13. Predicted increase in the fraction of total emissions that add to atmospheric CO₂. Changes in the mean partitioning of emissions as simulated by the C⁴MIP models up to 2000 (black symbols) and for the entire simulation period to 2100 (red symbols). The letters represent the models as given in Table 7.4. The box shown by the dotted line is a constraint on the historical carbon balance based on records of atmospheric CO₂ increase, and estimates of total emissions (fossil fuel plus land-use emissions) and the oceanic uptake of anthropogenic CO₂ (Sabine et al., 2004a). The black and red diamonds show the model-mean carbon partitioning for the historical period and the entire simulation period respectively. The thick red line shows the mean tendency towards increasing airborne fraction through the 21st century, which is common to all models.

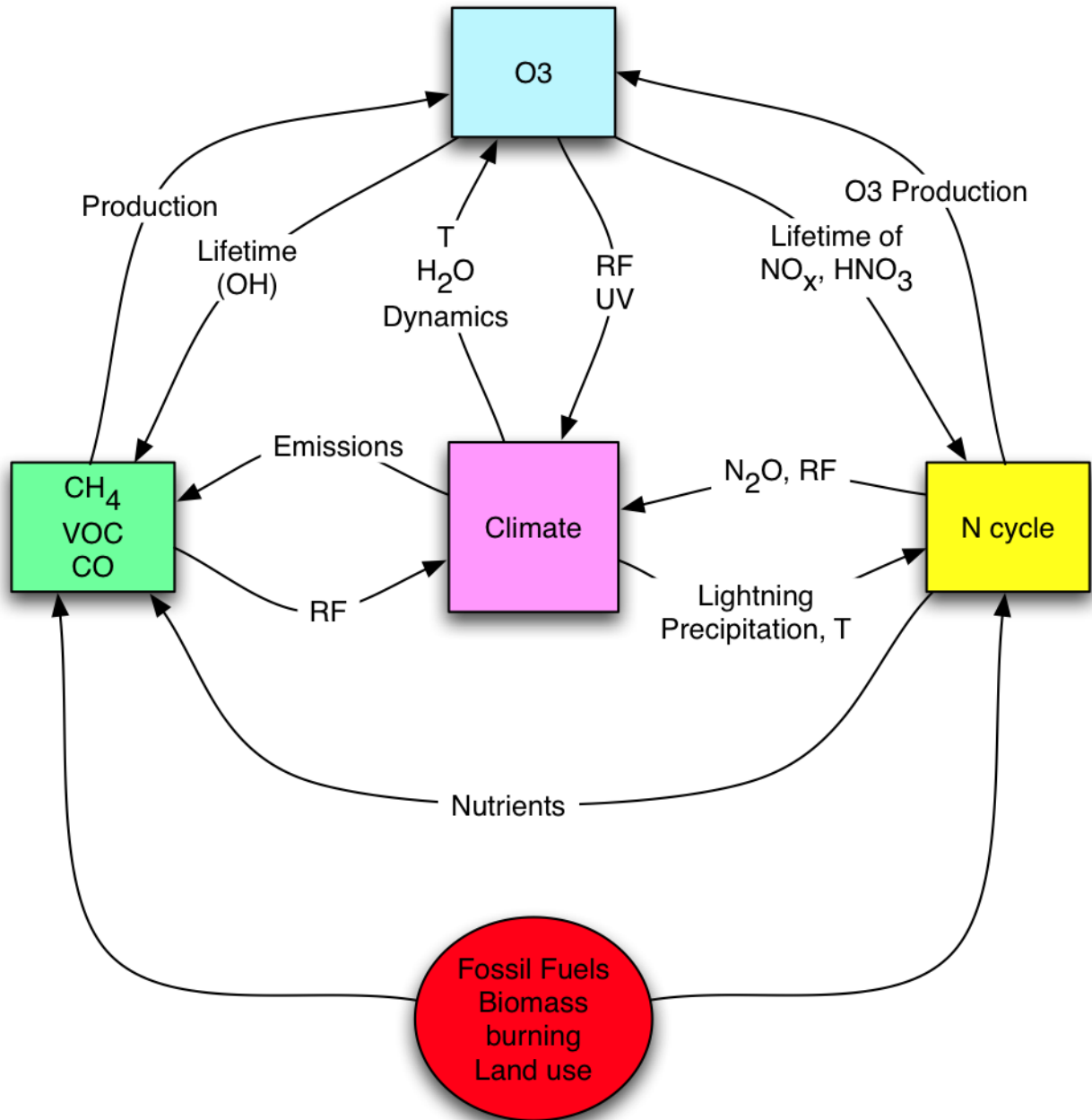
1
2



3
4
5
6
7
8
9
10
11

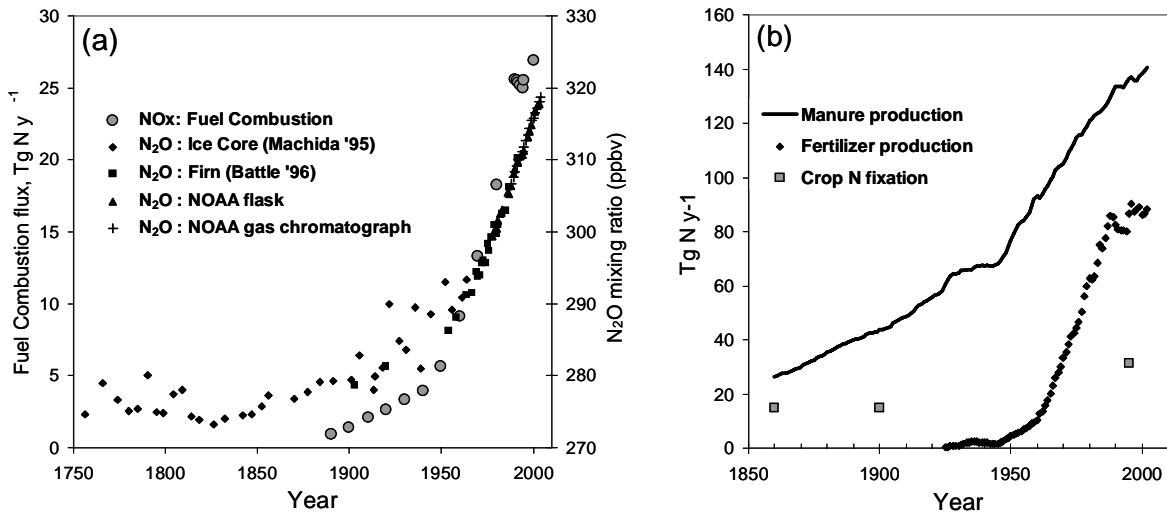
Figure 7.14. Uncertainties in carbon cycle feedbacks estimated from analysis of the results from the C⁴MIP models. Each effect is given in terms of its impact on the mean airborne fraction over the simulation period (typically 1860–2100), with bars showing the uncertainty range based on the ranges of effective sensitivity parameters given in Tables 7.4 and 7.5. The lower 3 bars are direct response to carbon dioxide increase (see Section 7.3.5 for details), the middle 4 bars show impacts of climate change on the carbon cycle, and the top black bar shows the range of climate-carbon cycle feedbacks given by the C⁴MIP models.

1
2



3
4 **Figure 7.15.** Schematic representation of the multiple interactions between tropospheric chemical processes,
5 biogeochemical cycles and the climate system. *RF* represents radiative forcing, *UV* ultraviolet radiation, and *T*
6 temperature.
7

1
2



3
4
5
6
7
8
9
10

Figure 7.16. (a) Changes in the emissions of fuel combustion NO_x and atmospheric N₂O mixing ratios since 1750. N₂O mixing ratios provide the atmospheric measurement constraint on global changes to the nitrogen cycle. (b) Changes in the indices of global agricultural nitrogen cycle since 1850: the production of manure, fertilizer and estimates of crop nitrogen fixation. For data sources see <http://www-eosdis.ornl.gov/> (Holland et al., 2005b) and [<http://www.cmdl.noaa.gov/>]. Figure adapted from Holland et al. (2005c).

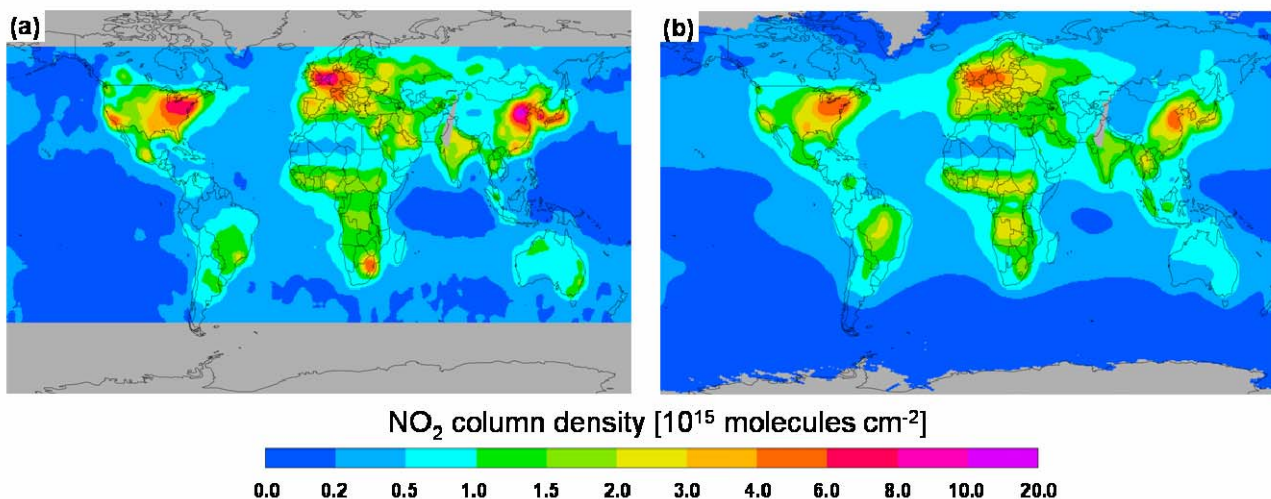
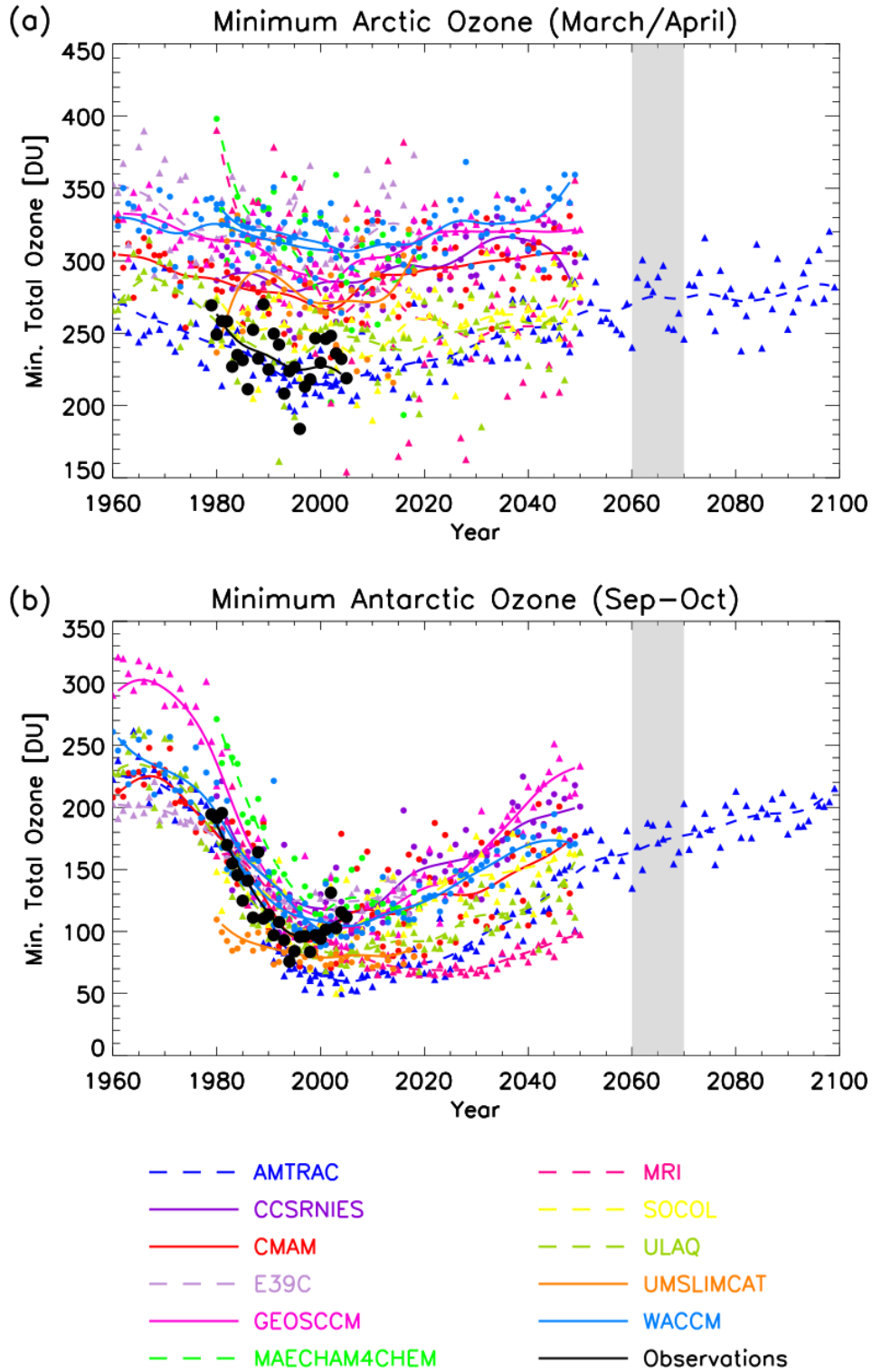
1
23
4
5
6
7
8
9
10
11

Figure 7.17. Tropospheric column NO₂ from (a) satellite measurements and (b) atmospheric chemistry models. The maps represent ensemble average annual mean tropospheric NO₂ column density maps for the year 2000. The satellite retrieval ensemble comprises three state-of-the-art retrievals from the Global Ozone Monitoring Experiment (GOME); the model ensemble includes 17 global atmospheric chemistry models. These maps have been obtained after smoothing the data to a common horizontal resolution of 5° x 5° (adapted from van Noije et al., 2006).

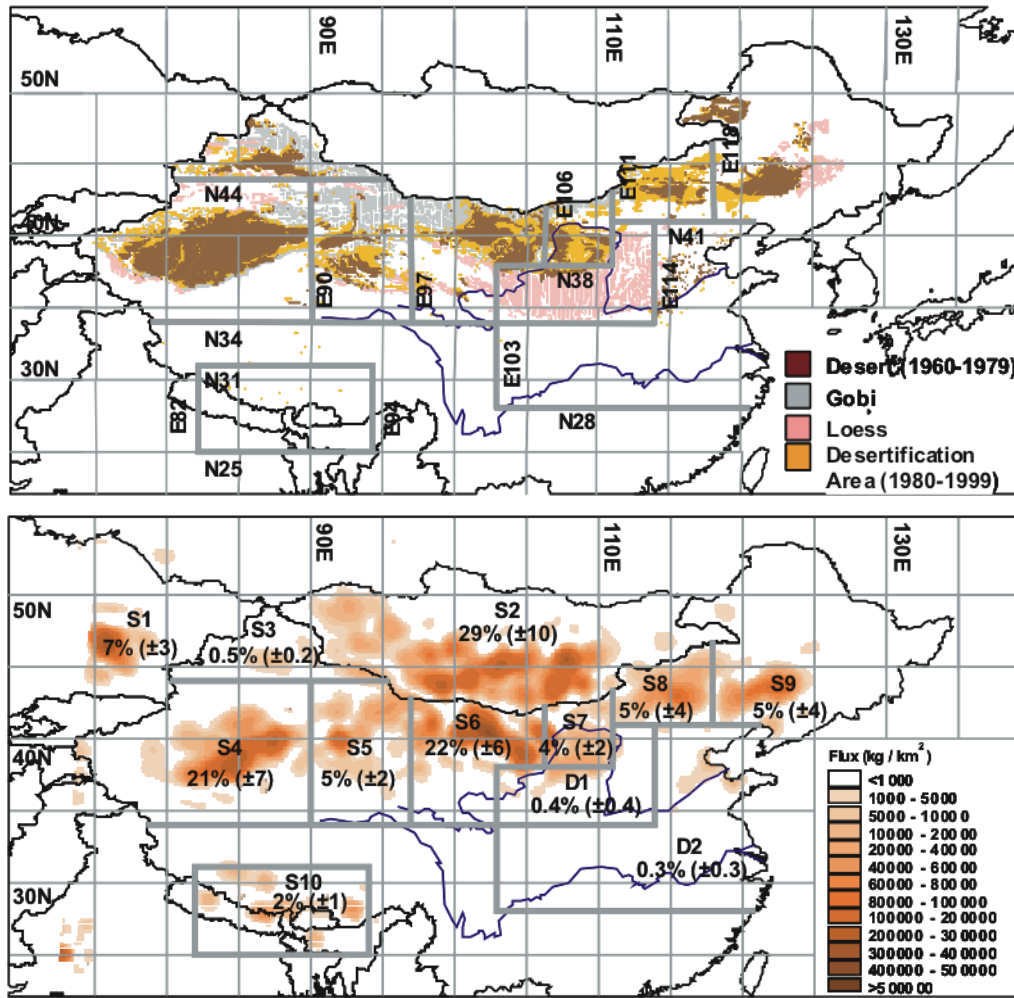
1
2



3
4
5
6
7
8
9
10
11
12

Figure 7.18. (a) Minimum Arctic total column ozone for March to April and (b) minimum Antarctic total column ozone for September to October (both poleward of 60°) in Dobson Units (DU). Simulations of future evolution of ozone were performed by 11 CCMs analyzed as part of the Chemistry-Climate Model Validation Activity for SPARC (CCMVal, <http://www.pa.op.dlr.de/CCMVal/>). Model results are compared with values calculated from the NIWA assimilated total column ozone data base shown as black dots (Bodeker et al., 2005). The light grey shading between 2060 and 2070 shows the period when halogen amounts in polar lower stratosphere are expected to return to 1980 values.

1
2
3



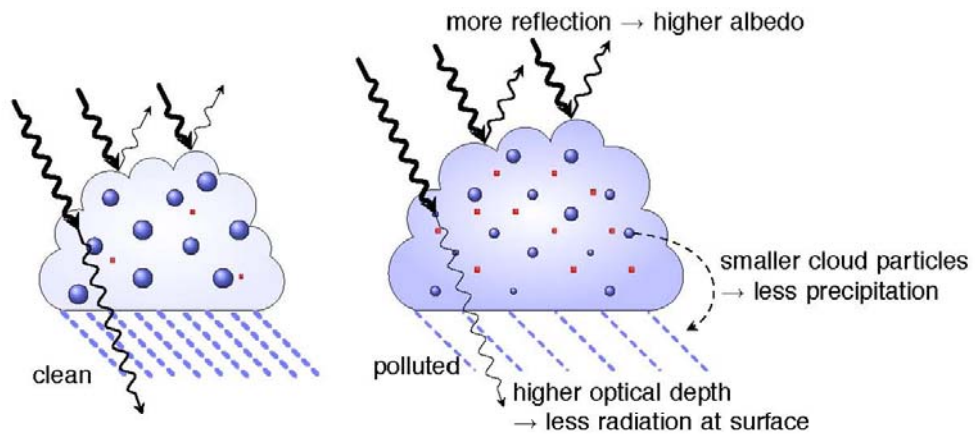
4

5
6
7
8
9
10
11
12
13
14
15

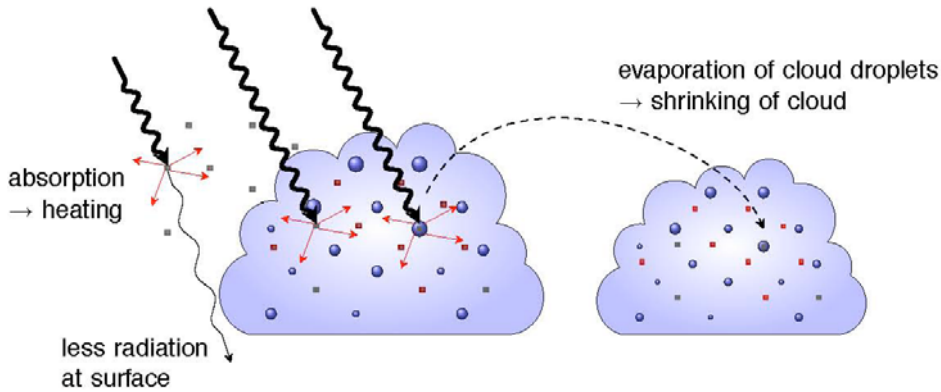
Figure 7.19. (a) Chinese desert distributions from 1960–1979 and desert plus desertification areas from 1980–1999; (b) Sources (S1 to S10) and typical depositional areas (D1 and D2) for Asian dust indicated by spring average dust emission flux ($\text{kg km}^{-2} \text{ month}^{-1}$) averaged over 1960–2002. The percentages with standard deviation in the parenthesis denote the average amount of dust production in each source region and the total amount of emissions between 1960–2002. The deserts in Mongolia (S2) and in western (S4) and northern (S6) China (mainly the Taklimakan and Badain Juran, respectively) can be considered as the major sources for Asian dust emissions. Several areas with more expansions of deserts (S7, S8, S9 and S5) are not key sources. Adapted from Zhang et al. (2003).

1
2

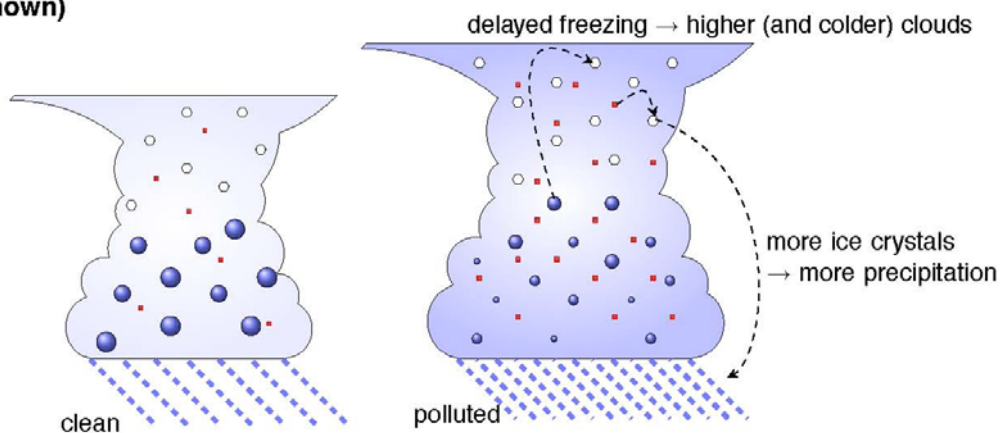
Cloud albedo and lifetime effect (negative radiative effect for warm clouds at TOA; less precipitation and less solar radiation at the surface)



Semi-direct effect (positive radiative effect at TOA for soot inside clouds, negative for soot above clouds)



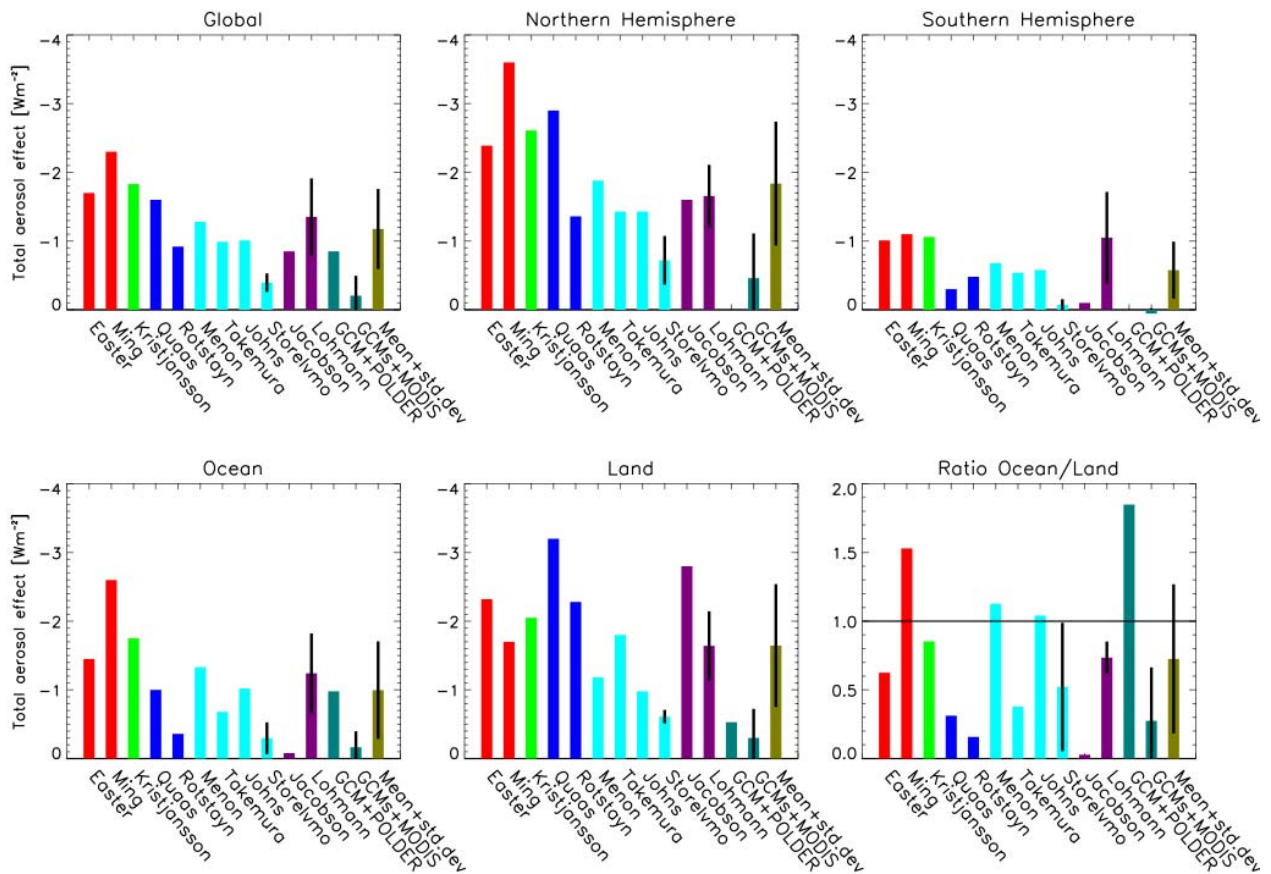
Glaciation effect (positive radiative effect at TOA and more precipitation), thermodynamic effect (sign of radiative effect and change in precipitation not yet known)



3
4
5
6
7

Figure 7.20. Schematic diagram of the aerosol effects discussed in Table 7.10. TOA refers to the top-of-the-atmosphere.

1
2



3
4

Figure 7.21. Global mean total anthropogenic aerosol effect (direct, semi-direct and indirect cloud albedo and lifetime effects) defined as the response in net radiation at the top-of-the-atmosphere from pre-industrial times to present-day and its contribution over the Northern Hemisphere (NH), Southern Hemisphere (SH), over oceans and over land, and the ratio over oceans/land. Red bars refer to anthropogenic sulphate (Easter et al., 2004; Ming et al., 2005⁺), green bars refer to anthropogenic sulphate and black carbon (Kristjánsson, 2002^{*,+}), blue bars to anthropogenic sulphate and organic carbon (Quaa et al., 2004; Rotstayn and Liu, 2005⁺), turquoise bars to anthropogenic sulphate, black, and organic carbon (Menon and Del Genio, 2005; Takemura et al., 2005; Johns et al., 2006; Storelvmo et al., 2006), dark purple bars to anthropogenic sulphate, black, and organic carbon effects on water and ice clouds (Jacobson, 2006; Lohmann and Diehl, 2006), teal bars refer to a combination of GCM and satellite results (ECHAM+POLDER, Lohmann and Lesins, 2002; LMDZ/ECHAM+MODIS, Quaa et al., 2005) and olive bars to the mean and standard deviation from all simulations. Vertical black lines for individual results refer to \pm one standard deviation in case of multiple simulations/results.

* refers to estimates of the aerosol effect deduced from the shortwave radiative flux only

⁺ refers to estimates solely from the indirect effects

20

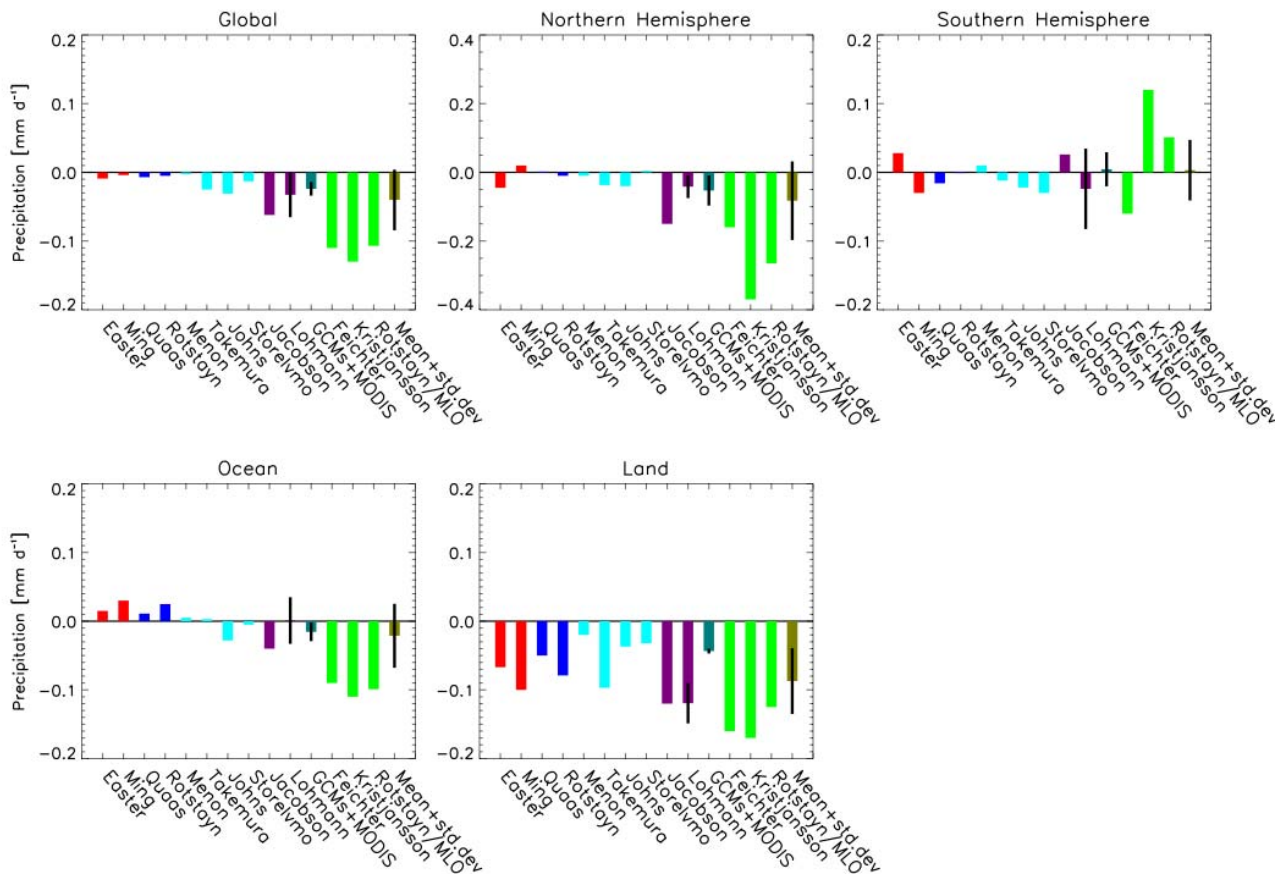
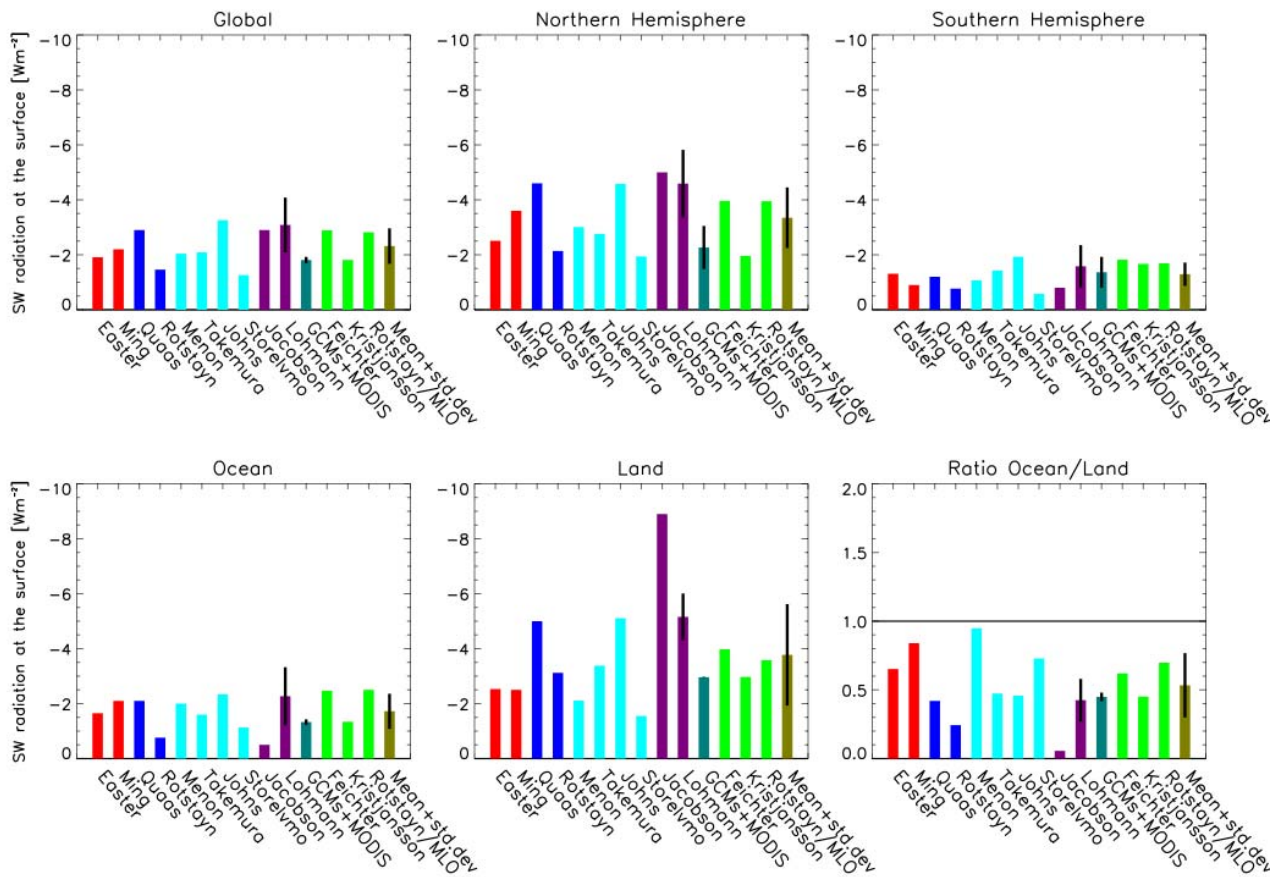
1
23
4
5
6
7
8
9
10
11
12
13
14
15
16
17
18
19

Figure 7.22. Global mean change in precipitation due to the total anthropogenic aerosol effect (direct, semi-direct and indirect cloud albedo and lifetime effects) from pre-industrial times to present-day and its contribution over the Northern Hemisphere (NH), Southern Hemisphere (SH) and over oceans and over land. Red bars refer to anthropogenic sulphate (Easter et al., 2004; Ming et al., 2005⁺), blue bars to anthropogenic sulphate and organic carbon (Quaas et al., 2004; Rotstajn and Liu, 2005⁺), turquoise bars to anthropogenic sulphate, black, and organic carbon (Menon and Del Genio, 2005; Takemura et al., 2005; Johns et al., 2006; Storelvmo et al., 2006), dark purple bars to anthropogenic sulphate, black, and organic carbon effects on water and ice clouds (Jacobson, 2006; Lohmann and Diehl, 2006), teal bars refer to a combination of GCM and satellite results (LMDZ/ECHAM+MODIS, Quaas et al., 2005), green bars refer to results from coupled atmosphere/mixed-layer ocean (MLO) experiments (Feichter et al., 2004 - sulphate, black, and organic carbon; Kristjansson et al., 2005 - sulphate and black carbon; Rotstajn and Lohmann, 2002⁺ - sulphate only) and olive bars to the mean from all simulations. Vertical black lines refer to \pm one standard deviation.

⁺ refers to estimates solely from the indirect effects

1
2

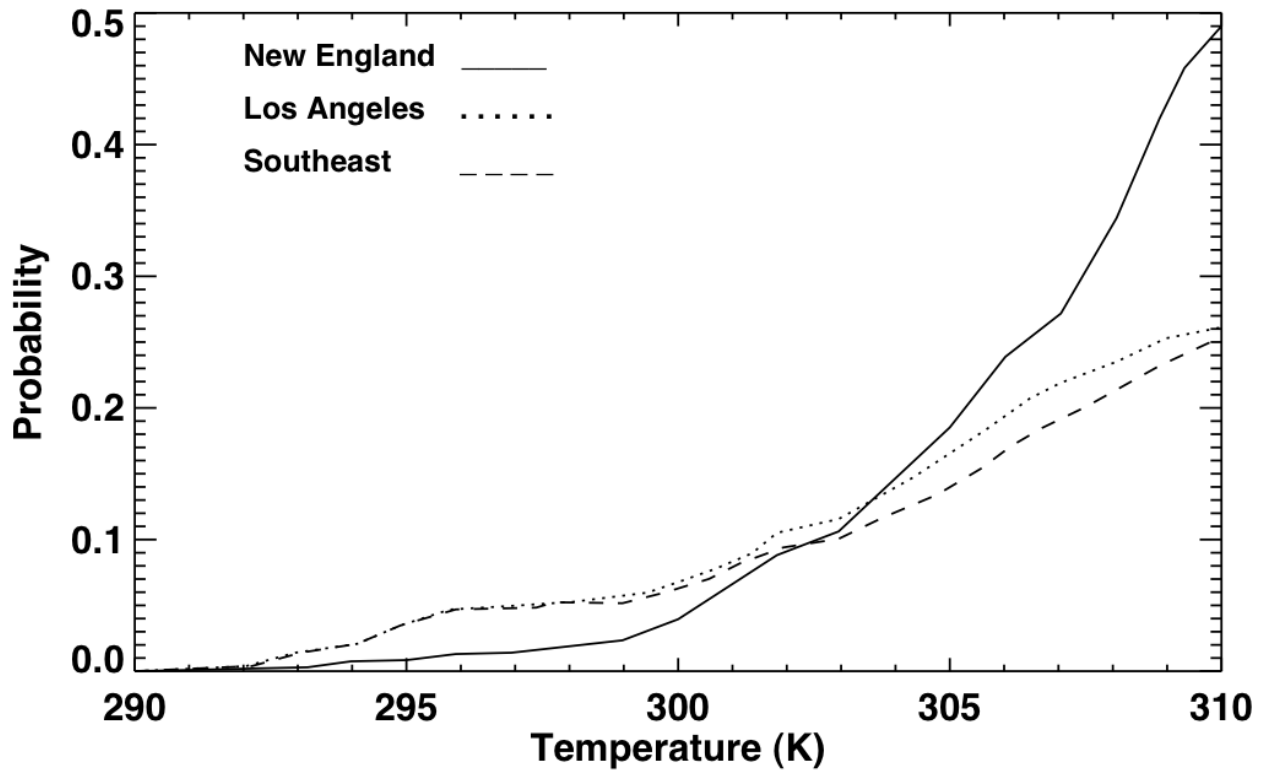


3
4

Figure 7.23. Global mean change in net solar radiation at the surface due to the total anthropogenic aerosol effect (direct, semi-direct and indirect cloud albedo and lifetime effects) from pre-industrial times to present-day and its contribution over the Northern Hemisphere (NH), Southern Hemisphere (SH), over oceans and over land, and the ratio over oceans/land. Red bars refer to anthropogenic sulphate (Easter et al., 2004; Ming et al., 2005⁺), blue bars to anthropogenic sulphate and organic carbon (Quaas et al., 2004; Rotstajn and Liu, 2005⁺), turquoise bars to anthropogenic sulphate, black, and organic carbon (Menon and Del Genio, 2005; Takemura et al., 2005; Johns et al., 2006; Storelvm et al., 2006), dark purple bars to anthropogenic sulphate, black, and organic carbon effects on water and ice clouds (Jacobson, 2006; Lohmann and Diehl, 2006), teal bars refer to a combination of GCM and satellite results (LMDZ/ECHAM+MODIS, Quaas et al., 2005), green bars refer to results from coupled atmosphere/mixed-layer ocean (MLO) experiments (Feichter et al., 2004 - sulphate, black, and organic carbon; Kristjansson et al., 2005 - sulphate and black carbon; Rotstajn and Lohmann, 2002⁺ - sulphate only) and olive bars to the mean from all simulations. Vertical black lines refer to \pm one standard deviation.

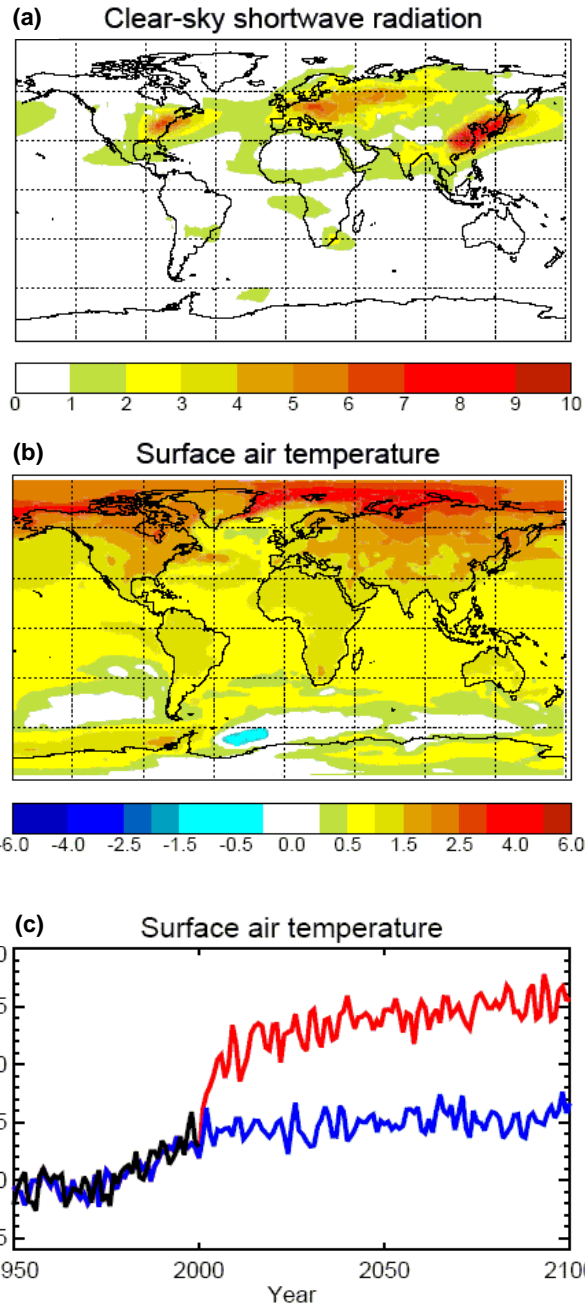
⁺ refers to estimates solely from the indirect effects

17
18
19

1
23
4
5
6
7
8
9
10

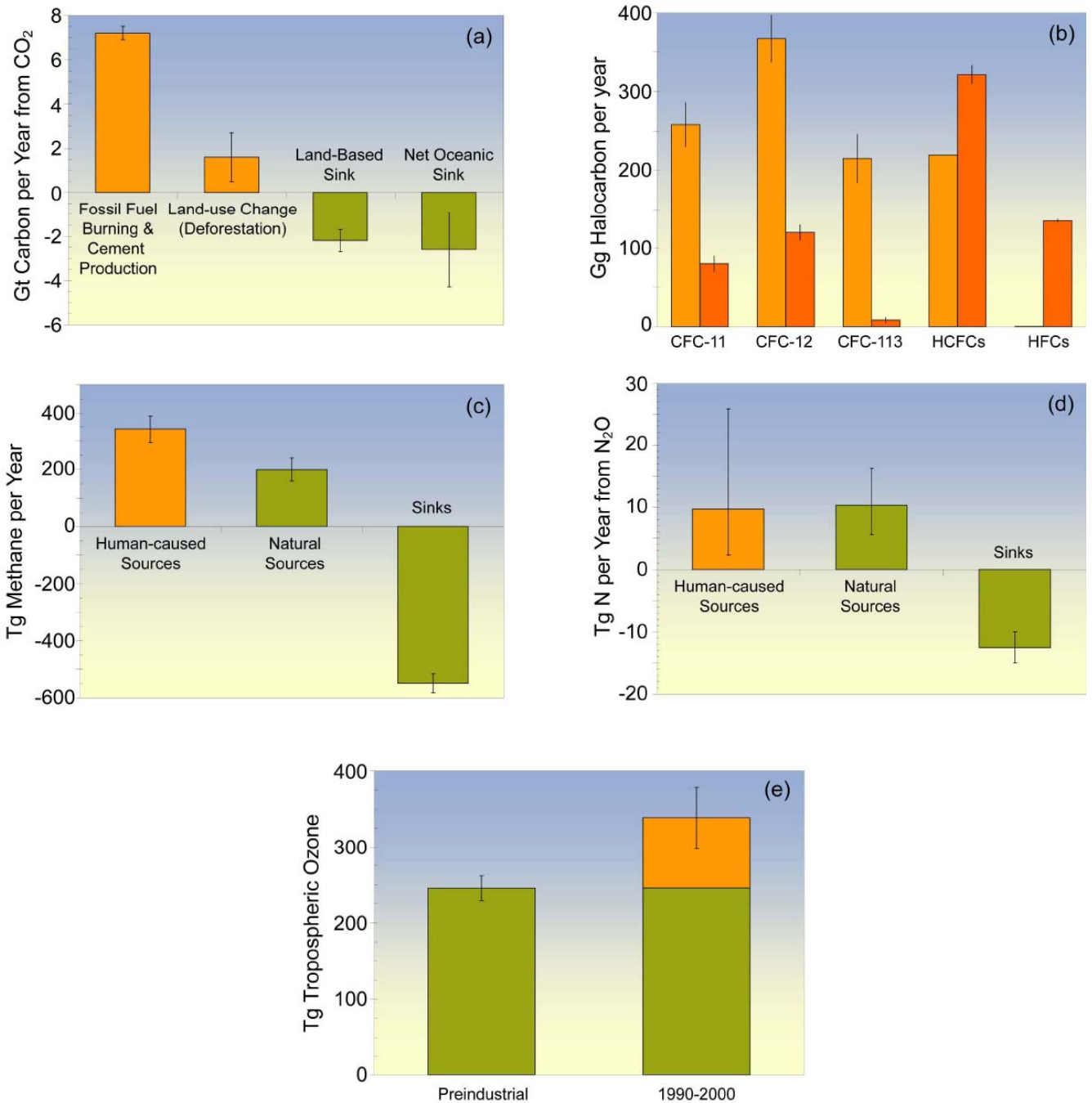
Box 7.4, Figure 1. Probability that the daily maximum 8-hour average ozone will exceed the U.S. National Ambient Air Quality Standard (NAQS) of 0.08 ppmv for a given daily maximum temperature, based on 1980-1998 data. Values are shown for New England (bounded by 36°N, 44°N, 67.5°W, and 87.5°W), the Los Angeles Basin (bounded by 32°N, 40°N, 112.5°W, and 122.5°W) and the southeastern United States (bounded by 32°N, 36°N, 72.5°W, and 92.5°W). Redrawn from Lin et al. (2001).

1



2
3
4 **Figure 7.24.** Effect of removing the entire burden of sulphate aerosols in year 2000 on (upper panel) the annual
5 mean clear-sky top of the atmosphere shortwave radiation ($W m^{-2}$) calculated by Brasseur and Roeckner (2005)
6 for the time period 2071–2100, and (middle panel) on the annual mean surface air temperature ($^{\circ}C$) calculated
7 for the same time period. Lower panel: temporal evolution of global and annual mean surface air temperature
8 anomalies ($^{\circ}C$) with respect to the mean 1961–1990 values. The evolution prior to year 2000 is driven by
9 observed atmospheric concentrations of greenhouse gases and aerosols as adopted by IPCC (see Chapter 10).
10 For years after 2000, the concentration of greenhouse gases remains constant while the aerosol burden is
11 unchanged (blue line) or set to zero (red line). The black curve shows observations (Jones et al., 2001: Global
12 and hemispheric temperature anomalies 1856–2000 – land and marine instrumental records.
13 <http://cdiac.ornl.gov/trends/temp/jonescru/jones.html>).

1
2



3
4

FAQ 7.1, Figure 1. Breakdown of contributions to the changes in atmospheric greenhouse-gas concentrations, based on information detailed in Chapters 4 and 7. In (a) through (d), human-caused sources are shown in orange, while natural sources and sinks are shown in green. In (e), human-caused tropospheric ozone amounts are in orange while natural ozone amounts are in green.

5

(a) Sources and sinks of carbon dioxide (CO₂). Each year CO₂ is released to the atmosphere from human activities including fossil fuel combustion and land use change. Only 57–60% of the CO₂ emitted from human activity remains in the atmosphere. Some is dissolved into the oceans and some is incorporated into plants as they grow. 1 Gt = 10¹⁵g (1 billion metric tonnes). Land-related fluxes are for the 1990s, fossil fuel and cement fluxes and net ocean uptake are for the period 2000–2005. All values and uncertainty ranges are from Table 7.1.

6

(b) Global emissions of CFCs and other halogen-containing compounds for 1990 (light orange) and 2002 (dark orange). These chemicals are exclusively human-produced. In this panel, 'HCFCs' comprise HCFCs-22, -141b, and -142b, while 'HFCs' comprise HFCs-23, -125, -134a, and -152a. 1 Gg = 10⁹g (1000 metric tonnes). Most data is from reports listed in Chapter 2.

7

- 1
2 (c) Sources and sinks of methane (CH₄) for the period 1983 to 2004. Human-caused sources of methane include
3 energy production, landfills, ruminant animals (e.g., cattle and sheep), rice agriculture, and biomass burning. 1
4 Tg = 10¹²g (1 million metric tonnes). Values and uncertainties are the means and standard deviations for CH₄ of
5 the corresponding aggregate values from Table 7.7.
6
- 7 (d) Sources and sinks of nitrous oxide (N₂O). Human-caused sources of N₂O include the transformation of
8 fertilizer nitrogen into N₂O and its subsequent emission from agricultural soils, biomass burning, cattle, and
9 some industrial activities including nylon manufacture. Source values and uncertainties are the midpoints and
10 range limits from Table 7.8. N₂O losses are from Chapter 7.
11
- 12 (e) Tropospheric ozone in the 19th and early 20th centuries and the 1990–2000 period. The increase in
13 tropospheric ozone formation is human-induced, resulting from atmospheric chemical reactions of pollutants
14 emitted by burning of fossil fuels or biofuels. The preindustrial value and uncertainty range are from Table 4.9
15 of the TAR, estimated from reconstructed observations. The present-day total and its uncertainty range are the
16 average and standard deviation of model results quoted in Table 7.10 in this report, excluding those from the
17 TAR.
18
19